Master Thesis

Reactively sputtered high-entropy carbide thin films based on Al-Cr-Nb-Ta-Ti

carried out for the purpose of obtaining the degree of Dipl.-Ing., submitted at Vienna University of Technology, **Faculty of Mechanical and Industrial Engineering**, by

Thomas Astecker, BSc

Matr.No.: 11740067

Looh 29, 4861 Aurach am Hongar, Austria

under the supervision of

Univ.Ass. Dipl.-Ing. Dr.techn. Alexander Kirnbauer

and

Univ.-Prof. Dipl.-Ing. Dr. mont. Paul Heinz Mayrhofer

Vienna, May 2023

_____

Signature

I confirm that the printing of this thesis requires the approval of the examination board.

Affidavit

I declare in lieu of oath, that I wrote this thesis and carried out the associated research myself, using only the literature cited in this volume. If text passages from sources are used literally, they are marked as such.

I confirm that this work is original and has not been submitted for examination elsewhere, nor is it currently under consideration for a thesis elsewhere.

I acknowledge that the submitted work will be checked electronically-technically using suitable and state-of-the-art means (plagiarism detection software). On the one hand, this ensures that the submitted work was prepared according to the high-quality standards within the applicable rules to ensure good scientific practice "Code of Conduct" at the TU Wien. On the other hand, a comparison with other student theses avoids violations of my personal copyright.

Place and Date *Signature*

Acknowledgements

I wish to express my sincere thanks to Univ.-Prof. Dipl.-Ing. Dr. mont. Paul Heinz Mayrhofer, head of the research group, for giving me the chance to write this thesis and for providing me with all the necessary facilities for the research as well as his exceptional knowledge in the field of material science. It was also him that initially attracted me to the topic of material science with his lectures at TU Vienna.

To the same extent, I want to thank my thesis adviser Univ.Ass. Dipl.-Ing. Dr.techn. Alexander Kirnbauer for supporting me throughout this research work. I am indebted to him for sharing his expertise as well as valuable guidance and encouragement given to me. He showed me how to approach research work in a proper way and how to tackle emerging difficulties along the way.

I also take this opportunity to express gratitude to all of the members of the Thin Film Group at TU Wien for their kindness and welcoming attitude.

Of course, I also want to thank my parents, for their encouragement, support, and attention throughout my studies and all other activities I like to undertake. Without them I would not be the person I am right now.

Last but not least, I would like to thank all my friends and fellow students, who were always good for a laugh and made these years of study unforgettable times. Cheers!

Table of Contents

Abstract

Due to the ongoing technological progress the need for high performance materials with special characteristics is rising. To satisfy this demand, in the case of metals, the pure elements are often not sufficient. Thus, almost every component in modern engineering consists of alloyed materials with specially tailored properties for the intended field of use. Traditionally alloying is the combination of one primary element with only small amounts of one or two secondary elements. This concept has shown the capability to produce adequate compositions for a wide variety of applications. However, research on a new concept of "high-entropy alloys", or in short, HEAs was started a few decades ago. The basic idea of this new approach, in contrast to traditional alloys, was that many contributing elements in equal or near equal amounts can be beneficial for the properties of the alloys.

Besides the composition of the bulk material, the performance of a component is also determined by the surface. To alter mechanical, electrical, chemical, or optical properties of a part's surface, the application of thin films with thicknesses in the micro or even nanometer range is a valuable approach. For such thin films as well as for the base materials HEAs are an interesting choice, promising potentially superior qualities.

This thesis is focuses on thin films based on "high-entropy carbides", which are a subcategory of "high entropy ceramics", or in short, HECs. The specimens were synthesised by reactive magnetron sputtering of an equimolar AlCrNbTaTi composite-target with acetylene mixed into the argon working gas. Additionally, varying amounts of silicon were added to the composition to show its effects on the mechanical properties as well as oxidation behaviour. The produced films were investigated by X-ray diffraction, nanoindentation testing, scanning electron microscopy, and X-ray fluorescence spectroscopy.

The reactively sputtered AlCrNbTaTi carbides as well as its silicon alloyed variants possess a clear cubic structure with a lattice parameter of 4.380 Å. Concerning the mechanical properties, hardness values of around 30 GPa were achieved while indentation modulus was between 380 GPa and 450 GPa. Both showed a slight tendency to increase with the silicon content. Vacuum annealing treatments up to 800 °C showed no measurable effect on the microstructure of the films while the annealing in ambient air led to the formation of a rutile-structured oxide scale. A clear impeding effect of the silicon content on the oxide growth was discovered. The sample without additional silicon formed an up to 7.8 µm

thick oxide scale at a temperature of 800 °C while the sample with the highest Si content did not form a measurable scale at all.

Kurzfassung

Durch die voranschreitenden technischen Entwicklungen steigt der Bedarf an Hochleistungswerkstoffen mit speziellen Eigenschaften stätig. Da jedoch die puren Metalle nur äußerst selten fähig sind diese Anforderungen zu erfüllen werden heutzutage fast ausschließlich Legierungen verwendet, welche es ermöglichen die Materialeigenschaften genau auf das betreffende Einsatzgebiet abzustimmen. Traditionell wird in Legierungen meist ein primäres Element mit geringen Anteilen eines oder zweien sekundären Elementen kombiniert. Dieses Konzept hat bereits bewiesen viele verschiedene Materialeigenschaften erzeugen zu können, womit die meisten Anwendungsfelder abgedeckt werden können. Dementgegen wurde vor wenigen Jahrzehnten mit der Forschung an sogenannten “Hoch-Entropie-Legierungen”, oder kurz, HEAs (high-entropy alloys) begonnen. Die Idee hinter diesem Konzept ist, dass, anders als bei bisherigen Materialien, viele Elemente in nahezu gleichen Anteilen in einer Legierung zu überlegenen Eigenschaften führen können.

Neben der Zusammensetzung des Grundmaterials hat unter Umständen auch die Beschaffenheit der Oberfläche großen Einfluss auf die Leistungsfähigkeit eines Bauteils. Ein gängiger Weg, um die Oberflächeneigenschaften zu modifizieren ist das Aufbringen mit einer Dünnschicht, die sinnvollerweise vom Grundmaterial abweichende mechanische, elektrische, chemische oder auch optische Eigenschaften besitzt. Auch als Beschichtungsmaterials sind HEAs aufgrund ihrer vielversprechenden Charakteristiken eine geeignete Wahl.

Diese Arbeit fokussiert sich auf die Synthese und Analyse von „Hoch-Entropie Karbiden“, welche eine Untergruppe der „Hoch-Entropie Keramiken“, oder kurz, HECs (high-entropy ceramics) darstellen. Die Proben wurden mithilfe von reaktivem Magnetron-Sputtern eines äquimolaren AlCrNbTaTi Targets hergestellt, wobei Acetylen zu dem inerten Prozessgas hinzugefügt wurde. Zusätzlich wurde der Einfluss von zusätzlichem Silizium in den Beschichtungen auf die mechanischen Eigenschaften und das Oxidationsverhalten untersucht. Um die abgeschiedenen Proben zu analysieren, wurde Röntgendiffraktometrie (XRD), Rasterelektronenmikroskopie (REM), Nanoindentation und Röntgenspektroskopie eingesetzt.

Die reaktiv gesputterten AlCrNbTaTi Karbide sowie die Varianten mit zulegiertem Silizium zeigen eine kubische Kristallstruktur mit einem Gitterparameter von 4.380 Å. Alle getesteten Proben besaßen eine Härte von in etwa 30 GPa während die Eindringmodule Werte zwischen 380 GPa and 450 GPa erreichten. Beide Kennzahlen zeigten eine leicht ansteigende Tendenz mit steigendem Siliziumgehalt. Die Mikrostruktur der Dünnschichten wurde durch Vakuumglühungen auf Temperaturen von bis zu 800 °C nicht messbar beeinflusst, während sich bei derselben Temperatur in Umgebungsluft Rutil-artige Oxidschichten bildeten. Ein deutlich hemmender Effekt des Siliziums auf das Wachstum der Oxide konnte festgestellt werden. Während die Schichten ohne Silizium bei 800 °C eine bis zu 7.8 µm dicke Oxidschicht, während die Proben mit dem höchsten Si-Gehalt bei derselben Temperatur keine messbare Oxidstärke erreichten.

List of figures

List of tables

List of Abbreviations and Symbols

CVD ..... *Chemical vapour deposition*

DC ..... *Direct current*

EDX ..... *Energy-dispersive X-ray spectroscopy*

HEA ..... *High-entropy alloy, High-entropy alloy*

HEC ..... *High-entropy ceramic*

PVD ..... *Physical vapour deposition*

SEM ..... *Scanning electron microscopy*

XRD ..... *X-ray diffraction*

XRF ..... *X-ray flourence spectroscopy*

1 Introduction

To create components and thin film coatings that can live up to high demands, the use of pure metals is usually insufficient. Thus, alloying has been the way to go for a considerable length of time. Through the combination of different elements, a wide span of different characteristics can be achieved.

Until two decades ago alloying typically involved a primary element combined with much smaller amounts of one or two secondary elements. Deviating from this classical approach, research on a new concept of multicomponent alloys was initially started by Brian Cantor in 1981 and many others have contributed to the investigation of the subject since then [1, 2]. The fundamental concept of this novel approach, in contrast to traditional alloys, was that many contributing elements in equal or near equal amounts can lead to favourable characteristics, contrary to the established opinion. In the year 2004 Jien-Wei Yeh introduced a definition for such compounds involving the mixing entropy and at the same time he also established the term “high-entropy alloys” [3] . In theory such materials can reach superior characteristics and have already shown to surmount typical alloys in practical applications.

In recent years, the concept has been extended to the field of “high-entropy ceramics”. Highly promising results have already been achieved there, yet only little research has been done compared to high-entropy alloys.

The utilisation of hard protective coatings to improve the characteristics of a highly stressed component is a widely used technology in modern mechanical engineering. A typical example is the application of titanium-based nitrides to elongate the lifespan of a milling tool which is obviously of great interest for manufacturers to safe costs [4]. Ideally, not only the mechanical properties are enhanced, but also the thermal characteristics allowing a tool to work at higher speeds for instance. But cutting tools are by far not the only application. Coatings can affect the properties of a part, or rather its surface, not only mechanically and thermally but also electrically, chemically, or optically [4]. Next to the economics, the use of coatings is also a valuable strategy to save resources and hence an important part of eco-friendly engineering.

Besides proven alloys like Ti-based nitrides for protective applications, whose evolution has already reached a saturated state, high-entropy alloys can also be the material of choice in coating technology opening a wide range of unique and unexplored possibilities

[5]. Concerning the ternary AlCrNbTaTi alloying system investigated in this work, promising properties, especially for high temperature applications, have already been achieved for nitride and oxide variants [6, 7].

The many different processes for the synthesis of thin films can be associated with the fundamental principles physical vapour deposition (PVD) and chemical vapour deposition (CVD). In PVD the material is vaporised through a physical process like heating or momentum transfer and condensed onto a substrate. In contrast, a CVD process already starts with a gaseous species which usually is reduced or decomposed onto the substrate [4]. A CVD process generally involves higher complexity compared to PVD where deposition temperatures are generally lower and material choice is less restricted. However, films prepared with CVD often show superiority when coating irregular shapes regarding thickness uniformity and porosity [4].

In this study high-entropy carbide thin films based on AlCrNbTaTi were deposited using reactive magnetron sputtering which is included amongst the group of PVD processes. Thereby, contrary to standard sputtering which takes place in an inert atmosphere, reactive gases like nitrogen, oxygen, methane, or acetylene are introduced and subsequently incorporated in the deposited film.

Furthermore, vacuum annealing treatments as well as oxidation studies were carried out on the synthesised samples. The outcome of these experiments besides the as-deposited films were investigated by nanoindentation testing, X-ray diffraction (XRD), scanning electron microscopy (SEM) and X-ray spectroscopy (XRF, EDX).

2 High-Entropy Alloys

Alloying has long been used to tailor the properties of materials to meet the requirements demanded by their intended field of use. Components in high-tech applications usually must withstand high mechanical loads and possess high chemical stability while being situated in high temperature environments. To create such durable parts, alloys are the way to go. Conventional alloying involves the combination of mostly one primary element with at least one or a few secondary elements in significantly smaller amounts.

However, almost two decades ago a new alloying concept gained the attention of material scientists. The novel concept involves combination of multiple principal elements in high concentrations to create new materials that could exceed the properties of existing materials. Compositions created by using this approach are generally known under the term “high-entropy alloys”, or in short HEAs. As this is a rather new concept, only tiny regions have been investigated so far. In theory, a very wide range of different material characteristics are attainable through this approach. Several HEAs have already been shown to exceed properties of conventional alloys and presumably there will be many more in the future [8].

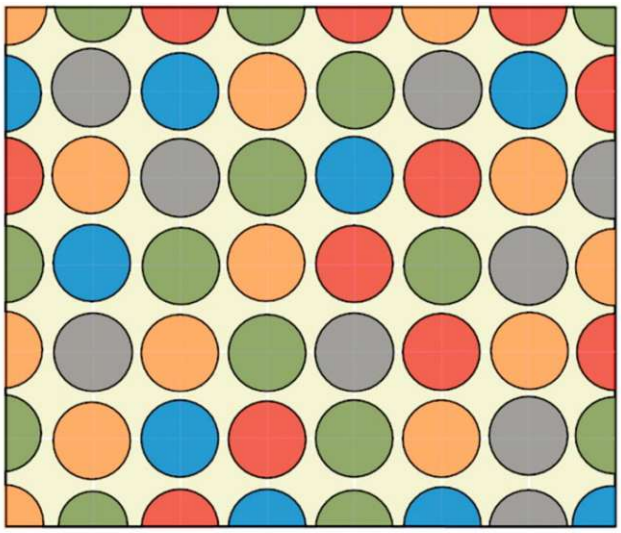

Fig. 1 Illustration of random mixing concept, where the circles in varied colours represent the different elements. Taken from [9].

2.1 Misunderstandings

Originally it was common sense in material science that adding multiple elements in large amounts to an alloy could very likely lead to topological disorder or the formation of intermetallic phases between the contributing elements. Such intermetallic phases are often characterised by a unique complex structure with high hardness linked with brittleness and a lack of feasibility, or in other words, not the characteristics material scientists are eager to attain. As a result of these phenomena so far, research focused on alloys consisting of only one or a few basic elements with much smaller fractions of alloying elements to get the desired material properties.

After Publications by Jien-Wei Yeh and Brian Cantor in 2004 it became apparent that a large number of contributing elements in equally large quantities can be beneficial or in some cases even superior to the traditional approach. The basic concept behind this is to create compositions that possess high mixing entropy to enhance the formation of solid solutions and reduce the number of phases, especially at higher temperatures. Simply put, against general opinions, combination of many principal elements does not necessarily lead to the formation of undesirable complex structures.

2.2 History

Initially, in 1981, research on multicomponent alloys was started by Brian Cantor and an ungraduated student of his. They performed studies on alloys with up to 20 different elements and even back then they were able to find a composition which forms a solid solution. In the following years, similar studies were performed by Cantor and his students. The conclusions of this studies were presented for the first time in the paper *Microstructural development in equiatomic multicomponent alloys* [10] in 2004. The contents of this paper were of great importance for the further investigation of multicomponent alloys, as Cantor provided significant findings about the phase formation of such compounds.

Furthermore, in the year 2004, Jien-Wei Yeh published important studies on multi-principal-element alloys or “high-entropy alloys” which further fuelled interest in this field [8]. Yeh first began research on multicomponent alloys in 1995, believing that the key to enhance mixing among components and reduce the number of phases is the mixing entropy. His studies in the following years supported this idea.

Since the publications by Cantor and Yeh the multicomponent or high-entropy alloying concept received increasing attention of scientists.

2.3 Thermodynamic Fundamentals – Entropy

To understand the fundamental idea behind HEAs, a basic understanding of the thermodynamic effects occurring during the mixing of multiple elements into an alloy is essential. The main attention when characterising the behaviour of thermodynamic systems lies on the Gibbs free energy G, which could also be interpreted as a thermodynamic potential. It is defined as follows,

$$\Delta G = \Delta H - \Delta S * T \tag{1}$$

where ΔH is the enthalpy of mixing, ΔS the entropy of mixing and T the thermodynamic temperature of the mixture. A system that performs no work except volume change work and is held at constant pressure and temperature will adopt the equilibrium state where the Gibbs free energy reaches its minimum [11]. Therefore, according to the definition stated above, a system must minimise enthalpy and maximise entropy, to reach such a state. Based on these relations, the Gibbs free energy can also be considered as an indicator for phase stability. The latter term of equation (1) also states that the influence of a high entropy of mixing on the stability of a phase is particularly significant the higher the temperature.

According to Zhang et al., the enthalpy of mixing, ΔH_{mix}, can be estimated by [12]

$$\Delta H_{mix} = \sum_{i=1, i\neq j}^{N} 4 * H_{AB}^{mix} * x_i * x_j \tag{2}$$

where H_{AB}^{mix} is the enthalpy of mixing for the binary equiatomic alloys and $x_{i,j}$ the corresponding atom concentrations of the participating elements N. Through empirical studies Zhang et al. found out that ΔH_{mix} normally is between -10 and 5 kJ/mol [12].

Furthermore, Otto et al. describe that two elements, which have the tendency to form a solid solution in a binary system, will maintain this behaviour for multi-component systems [13].

Regarding the entropy of mixing, for the sake of simplicity Yeh et al. ignore contributions of vibration, magnetic dipoles, and electronic randomness and consider only the configurational entropy as the entropy of mixing [3]. The configurational entropy of a N-component solid solution can be calculated by

$$\Delta S_{mix} = -R * \sum_{i=1}^{N} X_i * \ln(X_i) \tag{3}$$

where R represents the ideal gas constant and X_i the mole fraction of the i^{th} element. According to Yeh et al., when neglecting impacts of atomic size difference, mixing entropy, and mixing enthalpy are the main factors defining the equilibrium state. And while the mixing enthalpy defines whether a segregated state or a compound is formed, the mixing entropy is the main driving force to form a solid solution, especially at higher temperatures. These findings support the idea of having high numbers of participating elements in a mixture as it is done in the development of HEAs [8].

2.4 Definition

Debates about how to define if an alloy with a certain chemical composition can be classified as a HEA are still unsettled to this day. Originally Yeh et al. preferentially defined HEAs as alloys containing at least five principal elements with concentrations X_i reaching from 5 to 35 at%. In case there is a minor element in the alloy its atomic percentage X_j is hence less than 5 at%.

$$n_{principle} \geq 5 \quad 5\ at\% \leq X_i \leq 35\ at\%$$
$$n_{minor} \geq 0 \quad X_j \leq 5\ at\%$$

Later Yeh et al. also defined compositions showing configurational entropy at a random state larger than 1.5R, with R being the gas constant (R=8314 [J/(K*mol)]), as HEAs [8].

$$\Delta S_{mix} \geq 1.5R$$

Both definitions allow a large field of possible compositions to be considered as HEAs, though it is possible to attain alloys fitting to the former definition with configurational entropies lower than 1.5R. Equally it is possible, when creating mixtures with participation of considerably more principal elements than the defined minimum of five, to reach a mixing entropy larger than 1.5R when at the same time the percentages of principal elements is below the lower limit of 5 at% [8]. Yeh et al. still consider alloys as HEAs, even though one of the definitions is unfulfilled.

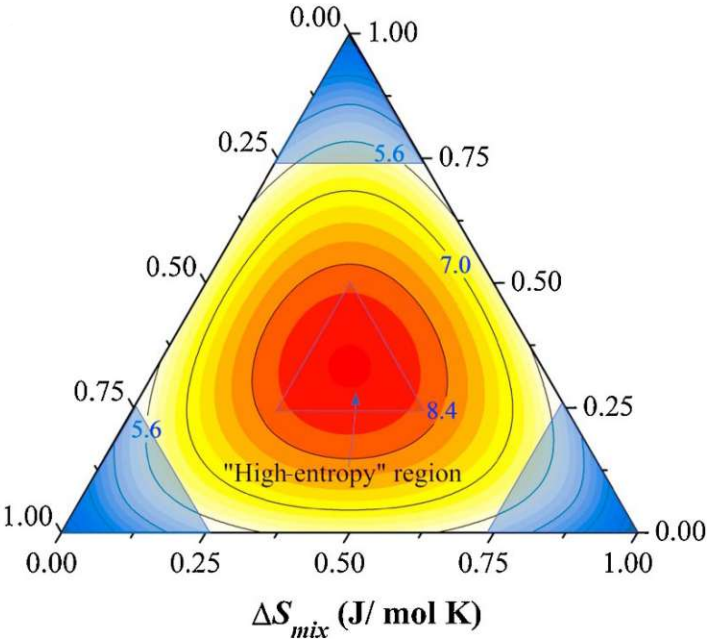

Fig. 2 Schematic plot of ΔS_{mix} of a ternary alloy system. The blue corners represent a conventional alloy, and the red region represents "high-entropy" alloys. Taken from [9].

Within the scope of this Thesis, HEAs are defined as compositions that are single-phase with a mixing entropy larger than 1.5R. This assumption is sustained by the fact that none of the traditional multicomponent alloys show mixing entropies larger than 1.5R [14].

2.5 The Four Core Effects

In their initial research work Yeh et al. established four core effects which should constitute the origin of the unique qualities attributed to HEAs [15]. Thereafter, these core effects have been pointing the way for many of the following research works.

2.5.1 High-Entropy Effect

The first effect, which was already mentioned in the preceding chapter, is the high-entropy effect. It suggests that the configurational entropy of a mixture is the dominant factor contributing to the Gibbs free energy and thereby facilitates the formation of solid solution phases, especially at elevated temperatures [15].

2.5.2 Lattice Distortion Effect

The number of different elements taking part in a HEA typically lead to strains in the structure because of size mismatch and varying bonding energies. This lattice distortion effect can have a range of different influences on the characteristics of a compound [8]. The most apparent consequence of distortions in the lattice is the strengthening effect caused by the internal stress fields which have an impeding effect on the dislocation slip.

2.5.3 Sluggish Diffusion Effect

Next, Yeh et al. defined the sluggish diffusion and the related slow phase transformation observed in HEAs as an important factor. Just as the lattice distortion effect it is also connected to the many different kinds of elements and their corresponding atoms that have to take part in a diffusion event [15].

2.5.4 Cocktail Effect

The last of the four core effects observed in HEAs is the cocktail effect which is also a factor in traditional alloys and is connected to interactions between the constituent elements and also the indirect impacts of some elements which can lead to unusual properties [8].

2.6 High-Entropy Ceramics

By including also non-metallic elements into a compound, the fundamental principle behind HEAs is extended to the field of "high-entropy ceramics", or in short HECs, whilst the same core effects promise vast potential. For HECs the definition mentioned above can be extended by considering not the configurational entropy of elements but that of the binary compounds instead. So, to be defined as HEC, an alloy must be single-phased and consist of at least five binary carbides, nitrides, oxides, borides, or sulphides [16].

If the configurational entropy of such compounds is calculated per formula unit, the criterium demanding a configurational entropy at a random state larger than 1.5R is met. Yet, to be precise, if the configurational entropy is calculated by atom, it becomes clear that the high entropy is only present at the metal sublattice. As a result of that, some researchers choose to designate HECs as high-entropy metal-sublattice carbides, nitrides, oxides, or borides [7, 17].

Compared to HEAs, the number of available variables for tuning the characteristics of the compositions is even higher in the case of HECs. Typically, such ceramics consist of carbides, nitrides, oxides, borides, or sulphides which have already proofed to possess high temperature stability in classically alloyed compounds [4]. But, besides mechanical or thermal properties, with HECs researchers have been able to achieve new properties, like colossal dielectric constant [18] or superionic conductivity at room temperature [19] which have not been found in HEAs, let alone traditional alloys, yet. Despite this fact, only little research is currently done on HECs compared to HEAs and groundbreaking results are still missing.

In the frame of this thesis high-entropy ceramic thin films based on AlCrNbTaTi were synthesised using reactive magnetron sputter deposition and subsequently analysed.

3 Thin Film Deposition

The application of thin films onto an object is a useful tool to influence its surface properties and thereby its capabilities in various ways. Thin films, by their nature, possess a very high surface to volume ratio and interestingly they can show substantially different qualities compared to the identical material in bulk form. Generally speaking, surface coatings that possess thicknesses in the range of several nanometres to a few micrometres are declared as thin films. Most of the processes used to deposit such films are, in contrast to bulk materials, non-equilibrium which means that the variety of achievable properties is less restricted. Also, the characteristics of a film are usually strongly dependent on the type of deposition technology and the specific process parameters used in the synthesis [4]. Yet, to put it simply, all deposition processes have the following three steps in common.

(i) Creation or transformation of the materials to deposit

(ii) Transportation from the source to targeted surface

(iii) Formation and growth of the film on the surface

Procedures that are used to apply thin layers of a material to a substrate or previously applied layers are summarised under the term “Thin Film Deposition”. Generally thin films are synthesised through additive procedures where materials are applied to the surface of a substrate either in the liquid state or in a gaseous form by condensation, reduction, or decomposition. Besides its composition, the quality of the film largely also depends on the physical state of the targeted surface, diffusion effects and binding energy between the substrate and film atoms.

In Fig. 3 a general overview of thin film deposition technologies is given. Wet processes are mostly characterised by their simplicity and applicability for a wide range of materials. These processes are essentially based on the application of a liquid precursor onto the targeted surface and a subsequent conversion into a finished coating. The two most important dry deposition principles are “Chemical Vapour Deposition” (CVD) and “Physical Vapour Deposition” (PVD), which can be further divided into a variety of different processes. However, all processes basically follow the same steps as mentioned before.

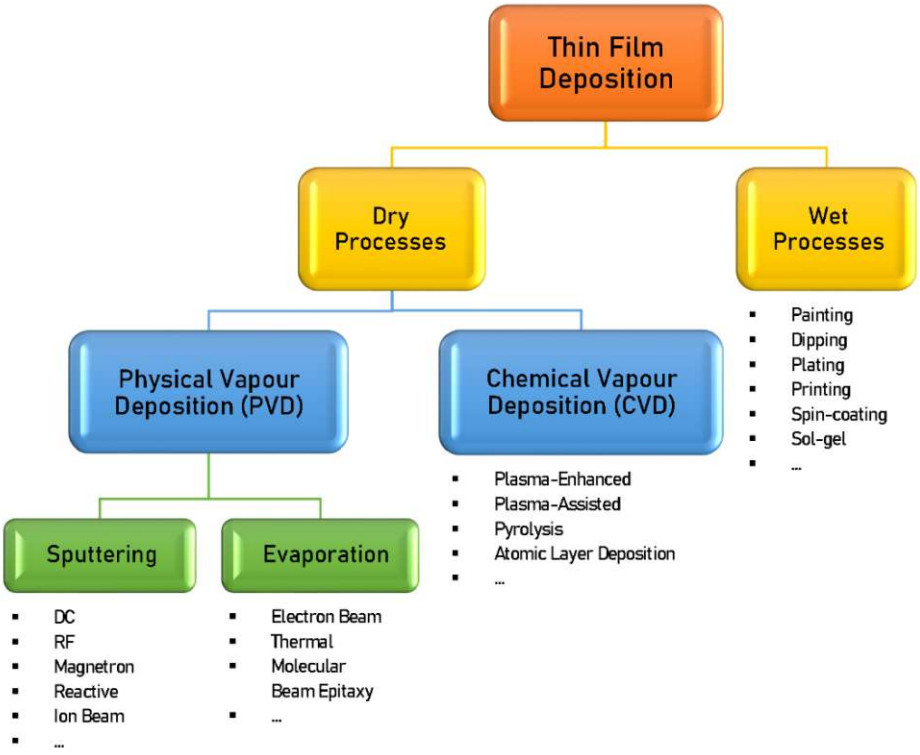

Fig. 3 Overview thin film deposition techniques (own work)

In a CVD process, thin films are produced by the decomposition or chemical reactions of gaseous reactants in an activated environment. Generally, such processes are more complex and run at much higher temperatures compared to PVD ones. Due to the high temperature requirement, there are some substrate materials not suitable for CVD coating processes.

Unlike in CVD processes, in PVD materials are transferred into a gaseous state through physical procedures. Subsequently the material is transported to the substrate surface where it proceeds to form a thin film.

In the framework of this thesis PVD was used to produce the investigated HEC thin films. Consequently, CVD processes will not be particularised further in the remaining work.

3.1 Physical Vapour Deposition

PVD processes can rely on different physical methods to transfer a solid target material into a gaseous state and subsequently force it lay down on a substrate resulting in the formation of a thin film. Yet, for all PVD variants, the target material initially exists in a solid state inside a vacuum chamber, but in the conversion to the gaseous state and the transportation to the substrate surface is where they differ.

Transformation from a solid material to a gaseous sate can be obtained in a variety of ways with thermal evaporation, electron beam evaporation, laser deposition, arc-evaporation or sputtering being the most common ones. After evaporation, the detached target atoms are moving through the vacuum disorderly or guided by electric fields until they impinge on a surface, preferably for the most part on the object intended to coat. After making contact with the surface the atoms have not reached their ultimate position yet. Diffusion processes start to take place where the particles strive to arrange in a way that is energetically favourable.

After the aspired film thickness is reached or, equivalently, the predefined deposition time is over the evaporation is stopped. Before the chamber is vented it is very important to make sure that the substrates are left to cool down to a temperature where uncontrolled oxidation does certainly not occur.

To improve the uniformity of the deposition rotation can be applied to the target or the substrate during the coating process. Especially for multidimensional objects, as cutting tools for example, this is inevitable.

For the AlCrNbTaTi carbide thin films addressed in this thesis, reactive planar magnetron sputtering was used to coat flat substrates. Therefore, this process will be explained in more detail in the following paragraphs.

3.2 Sputtering

Sputtering is a physical process, where atoms are ejected from a target material through bombardment with high energy particles, mostly ions. A schematic configuration of a sputtering system is illustrated in Fig. 4.

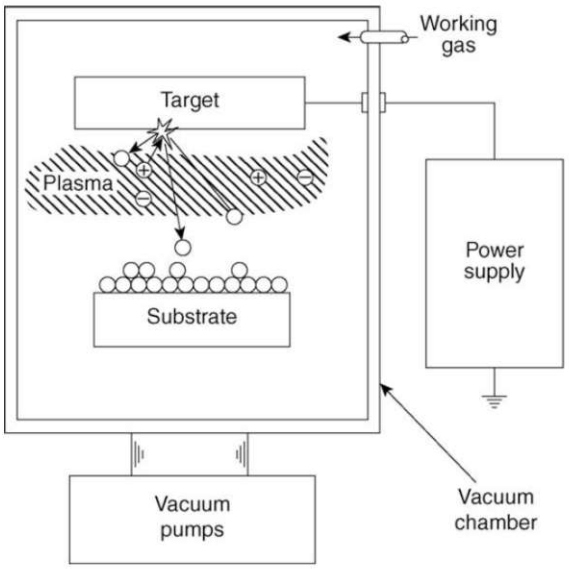

Fig. 4 Schematic representation of a basic sputtering process. Taken from [4].

To define how many particles are ejected compared to the impinging projectiles, the term sputter yield *Y* is introduced. This characteristic value depends mostly on target material, bonding energies, projectile material, and projectile energy [4, 20]. The relation between sputter yield and different target elements, bombarded by an argon ion at constant energy of 300eV, is shown in Fig. 5.

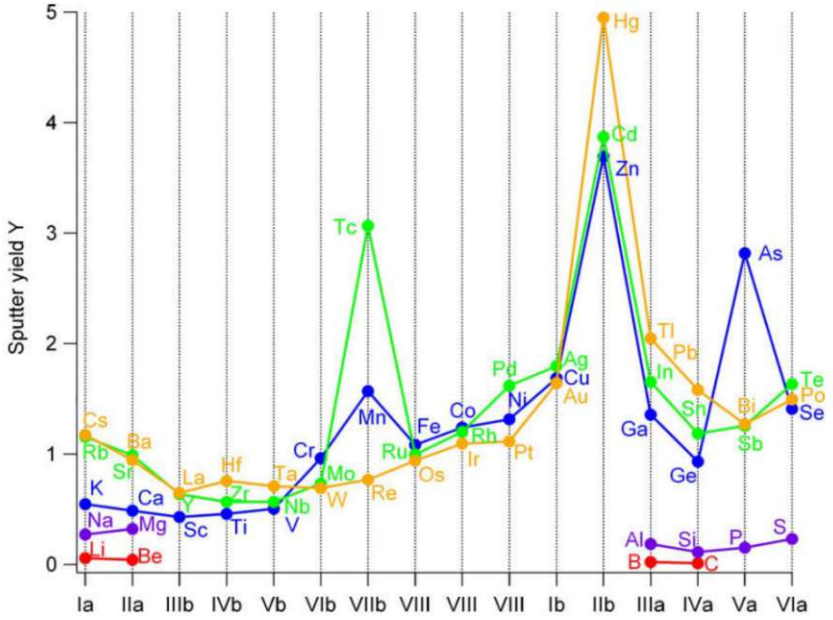

Fig. 5 Illustration of the sputter yield dependence of several target elements, when bombarded by a given ion at constant energy (calculated using SRIM). Taken from [4].

When conducting reactive sputtering processes, where reactive gases are mixed with the working gas, through effects like nitride or oxide formation on the target surface, the sputter yield can be dramatically decreased [21]. If this condition occurs the target is considered to be in a “poisoned” state.

Furthermore, when alloys are sputtered, the formation of the film on the substrate is influenced by weight and bonding energy of the participating elements. When a sputter atom of a heavier element impinges on the already formed film, it is likely that lighter or weakly bonded elements are knocked out of the surface. The formed film may consist of higher fractions of the heavier elements compared to the fractions present in the target material then [20].

For the production of high energy particles, commonly one of two concepts are followed. In the first approach the target material is sputtered by an ion gun aimed directly towards it. Secondly, a plasma can be utilised as a source of ions which are then attracted towards the target by applying a highly negative voltage [4]. Commonly, low-pressure argon plasmas are utilised for sputter deposition.

3.2.1 Direct Current Discharge

In direct current sputtering the target represents the cathode. If the substrate is grounded it represents the anode together with the rest of the vacuum chamber. In other configurations the substrate may be floating or biased with a small negative voltage. Through application of an electric field to an inserted inert gas, in most instances argon, a plasma is formed. This plasma nearly consists of similar numbers of negatively charged electrons and positively charged gas ions, which are accelerated towards the substrate or the target by the applied electric field, plus neutrals [22]. The impinging gas ions eject target atoms into the chamber which eventually form a thin film on the substrate. As there is a constant direct current applied between cathode and anode there is a constant ionisation, target bombardment and subsequent deposition on the substrate.

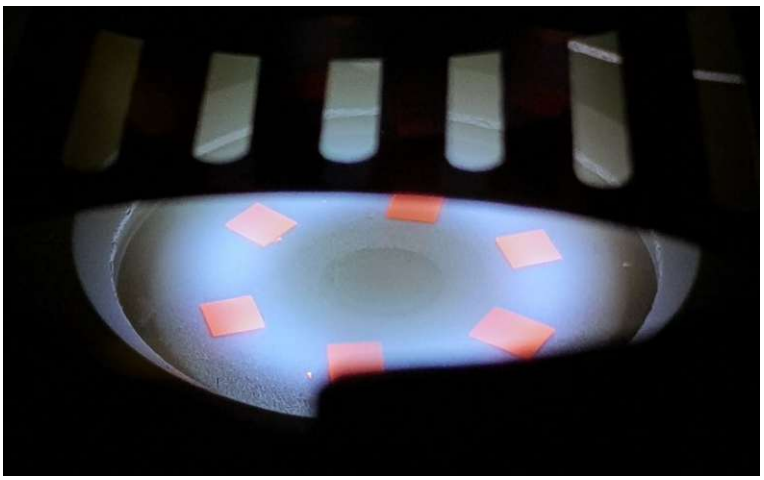

Fig. 6 DC discharge of a reactive magnetron sputtering process (silicon platelets placed on target).

The extent of ionisation in a discharge is generally defined by the number electron impacts competing with the loss of ionised particles through recombination or passage to the chamber walls. Consequently, the efficiency of the ionisation generally depends on the type of gas, the chamber pressure, and the strength of the electric field [4].

To improve the generally low efficiency of the ionisation and the related deposition rate in standard DC sputtering, for example magnetron sputtering is used. The perks of this add-on will be explained in detail in the succeeding chapter.

The ignition of a plasma from a initially insulating inert gas can be viewed as a sort of chain reaction. By appying a high DC voltage some random electron is accelerated towards the anode which will eventually hit a neutral gas atom and ionize it. Through charge

conservation, this process will create two new electrons which subsequently also ionise neutral atoms. The ionised atoms are then accelerated towards the cathode by the applied electric field. When they strike the target, they will sputter target atoms and produce secondary electrons. Through this processes the discharge finally becomes self-sustained [23].

As illustrated in Fig. 7, a DC glow discharge consists of optically distinguishable regions which are alternatingly glow or remain dark. The illumination in some regions arises form the de-excitation of positive ions, which leads to the emission of photons [23]. Therefore, glow is directly connected to the presence of electrons with sufficient energy to excite the working gas.

Directly adjacent to the cathode is a very thin dark layer called Aston dark space. The presence of this layer is only observed in noble gas discharges [24]. The lack of illumination can be connected to the electron energy which is still too low to produce ions.

Next is the cathode glow region where the secondary electrons generated by the bombardment of the target cathode now have gained sufficient energy to gereate excitation [24].

In the cathode dark space most of the discharge voltage is dropped which serves to accelerate the working gas ions towards the target. At the same time the electrons ,headed in the opposite direction, are not yet capable of producing excitation which explains the dark appearance of this region.

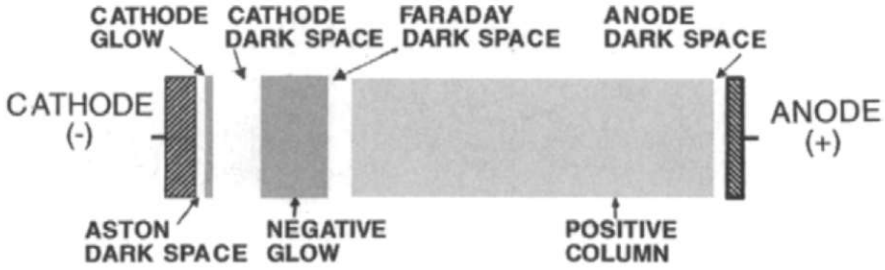

Fig. 7 Schematic representation of a DC glow discharge. Taken from [23].

After accelerating sufficiently in the cathode dark space, the electrons are now capable to create excitation events leading to photon emission in the negative glow region. In a sputtering process the substrate is usually placed in this region. Hence, the Faraday dark space as well as the positive column do not appear in such a process. There exists a dark

space adjacent to the anode which is connected to the complex charge distribution and the subsequent electron movements which diminish the gas excitation [24].

3.2.2 Magnetron Sputtering

In a magnetron sputtering process, an additional magnetic field is positioned behind the cathodic target. Through superposition of the electric and magnetic field, the charged particles are no longer moving parallel to the electric field lines, instead, they are circulating over the target surface (see Fig. 8). This increases the impacts per electron, because the electrons are captured in the discharge for longer which enables them to generate more ions compared to previously described standard DC discharge, while electron density remains the same. This allows discharge pressure and cathode sheath to be lowered, which leads to fewer collisions for the sputtered atoms before they reach the substrate. Furthermore, the inert gas ions will reach the cathode with almost full discharge voltage [4]. All in all, these effects lead do much higher deposition rates which is the reason why magnetrons are used in most DC sputtering processes.

Magnetrons exist in planar or cylindrical form, where planar ones are more common due to their convenience. For the coating process on behalf of this thesis, circular planar magnetrons were used.

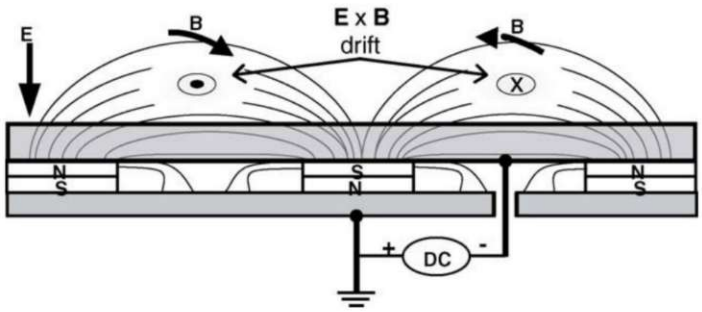

Fig. 8 Illustration of a planar magnetron sputtering target, where E is the electric field and B the magnetic flux density. Taken from [4].

As shown in Fig. 8, in a planar circular magnetron the plasma is restricted within annular rings over the target surface. This is magnetic field is obtained by placing a centre disk pole and an annular ring pole under the target material. As seen in the Fig. 8, the field strength varies over the surface and the direction of the field lines changes. This field shape forces the electrons towards the ring-shaped region between the magnets, leading

to higher ion production and particle ejection in this area which results in the characteristic erosion profile of abraded targets, the so-called “racetrack”. This could be considered as a drawback of magnetrons, because the available target surface is not utilised evenly.

3.2.3 Vacuum Conditions

In a sputter deposition process the importance of the chamber pressure cannot be emphasised enough. To minimise the incorporation of residual gas during the deposition of the film, the process pressure should be as low as possible. At the same time a higher vacuum reduces the number of collisions the sputtered atoms will undergo until they reach the substrate leading to a higher deposition rate. Additionally, the number of electron collisions is lowered allowing them to sustain their high kinetic energy which is essential to sustain the plasma.

Besides all that, there are other factors limiting the increase of the vacuum. By lowering the pressure, the efficiency of the ionisation will be decreased as fewer ionised gas particles are available to bombard the target. Eventually this will lead to a decrease in sputtering yield and deposition rate [22].

To summarise, there is a certain process pressure range where a plasma can be sustained and, additionally, there is an even narrower optimal range where the deposition rate and film quality reach their peak values.

3.2.4 Bias

To reach higher purity films with increased uniformity, a small negative potential can be applied to the substrate fixture during deposition. With this, a slight ion bombardment of the substrate is propagated and the already formed film is “resputterd” which can affect the film properties dramatically. The impinging ions may force the film surface to rearrange, leading to altered physical, chemical and electrical characteristics [4]. Also, weakly bound contaminations are removed, whereby the purity of the produced films is increased. The generally lower deposition rate on biased substrates is additionally decreased by the fact that the synthesised films usually possess a higher density as a result of the enhanced ion bombardment

It should be noted that it is important to make sure the applied bias voltage is chosen deliberately so that the wanted effect is achieved. Increased bias voltages can also be used to clean the substrate before the deposition process.

3.2.5 Reactive Sputtering

In reactive sputtering, a reactive gas is introduced into the deposition chamber in addition to the inert working gas. The ratio between reactive and working gas is typically rather low. During the deposition process the reactive gas chemically interacts with the sputtered target material to form a compound which is then deposited on the substrate. This allows to produce coatings with properties that strongly deviate from the classical metallic films. It is important to note that reactive sputtering is usually conducted with metallic target materials only. Even though identical films could be deposited non-reactively by using a target with the wanted compound, there are many drawbacks like a lower deposition rate and additionally the manufacturing as well as handling of such targets is generally more delicate as they tend to be very brittle compared to metallic targets [23]. The most common compounds produced by reactive sputtering are:

- Nitrides (nitrogen, ammonia)
- Oxides (oxygen)
- Carbides (methane, acetylene)
- Sulphides (hydrogen sulphide)

A characteristic problem of reactive sputter processes is the so-called “poisoning” occurring on the target surface. This effect is present if the chemical reactions of the target surface with the reactive gas are faster than the target erosion. The sputter rate of a poisoned target and further the deposition rate are typically lower than that of a metallic target. Additional problems arise if the compound formed on the target is non-conductive. Hence, in a reactive sputter process one should aim for a state where the target surface is still in a metallic state while a stoichiometric compound is formed on the substrate.

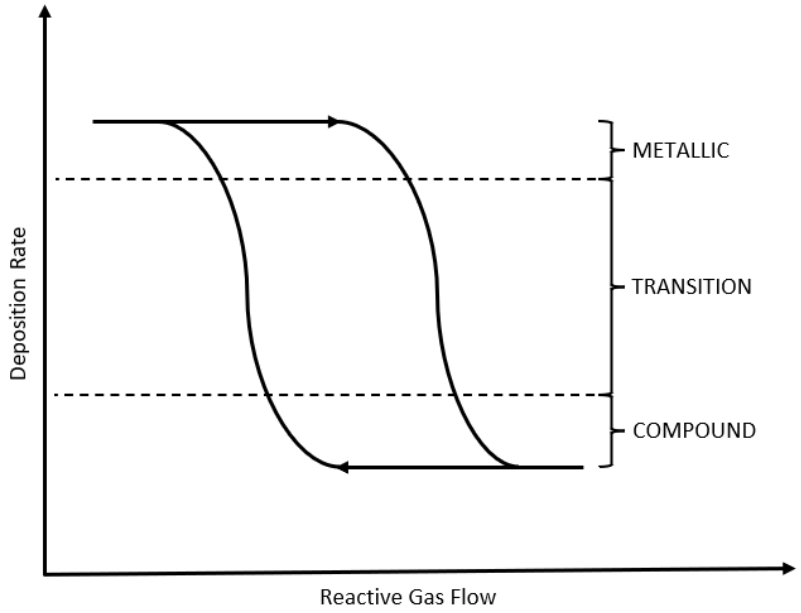

Fig. 9 Schematic representation of a hysteresis for deposition rate vs. reactive gas flow (own work).

To achieve this, the optimal reactive gas partial pressure can be determined by recording a hysteresis curve (see Fig. 9) for deposition rate vs. reactive gas flow.

To restore the metallic state of the target in case of poisoning, sufficient conditioning in pure argon, without the presence of reactive gas, is required.

4 Oxidation

Essentially, oxidation is a chemical reaction where the subject in question undergoes a loss of electrons which is synonymous with a rise of the oxidation state. The oxidation state or oxidation number are used to quantify the charge of an atom within a compound. Ultimately, oxidation of one substance leads to reduction, which stands for a decline in oxidation state or rather gain of electrons, of another substance. As the two processes cannot happen independently of one another they are usually referred to as redox reactions.

For metals and alloys oxidation in the form of thin oxide films can be highly beneficial in terms of enhancement of corrosion and wear resistance, especially at higher temperatures. Along with other elements aluminium is a very well-known example as it inherently forms a protective oxide layer when in contact with the oxygen in the atmosphere making it less affected by the environment.

The formation of oxide films is closely tied to diffusion processes and the properties of the base material. This means that the thickness and composition of the formed scales are largely dependent on temperature and time [14]. It should also be noted that the formation of an oxide is accompanied by the generation of stresses which can ultimately lead to cracking of the film. This phenomenon should be avoided as the protective vanishes in this case.

In the scope of this thesis, to examine the oxide formation behaviour, the deposited carbide films were oxidised by ambient air annealing at different temperature levels for varying time periods inside a chamber furnace.

5 Vacuum Annealing

Vacuum furnaces are commonly used to conduct high temperature heat treatments on metals and ceramics where contamination through the atmosphere must be inhibited. In the frame of this thesis vacuum heat treatments were conducted to investigate if thermally-induced phase transformations or microstructural modifications and related changes in the mechanical properties occur at certain temperature levels.

6 Investigative Methods

6.1 X-Ray Diffraction

X-ray diffraction (XRD) is used to determine the crystal structure of materials in a non-destructive way. The process is capable of providing information about the crystallinity, lattice-parameters, the crystal-structure, and crystal-orientation. Furthermore, even residual stresses can be monitored using XRD measurements.

Broadly speaking, the procedure is based on the ability of X-rays to penetrate through all different kinds of materials and the evaluation of their interactions with the atoms inside the irradiated substance.

6.1.1 Physical Background

The theoretical foundation of the examination of crystals through diffraction of X-rays is formed by Bragg's law. This law delivers angles for coherent as well as incoherent scattering from a crystal lattice. It was defined as follows.

$$n * \lambda = 2 * d * \sin(\theta) \tag{4}$$

Where n is a positive integer, λ is the wavelength, d is the interplanar distance and θ the glancing angle formed by the incident ray respectively the reflected ray and a lattice plane.

The law indicates that if an X-ray with the wavelength λ impinges on lattice planes with the interplanar distance d at an angle θ, it will be diffracted (see Fig. 10). This diffraction is a result of interdependencies of the X-ray with the electron shell, which is of a rather complex nature and will not be discussed further in this thesis.

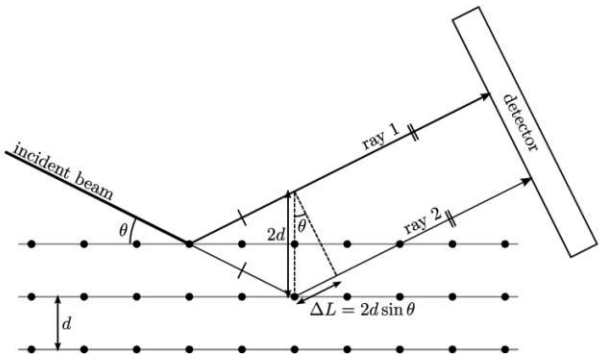

Fig. 10 Illustration of Bragg's Law. The incident beam comes from the left and gets partially reflected by each lattice plane, taken from [25].

Generally speaking, if the difference between the travelling distances of the rays is a multiple of the wavelength, the rays will stay in phase with each other after the diffraction. On the contrary, if Bragg`s law is not met, the emergent beams are no longer in phase which results in mutual weakening of the rays. As a result of the multitude of lattice planes, some out of phase reflected rays will exist, that annihilate other rays when they are overlapped.

6.1.2 Setup of an X-ray diffractometer

An X-ray diffractometer basically consists of an X-ray tube, a sample holder, and an X-ray detector. In the X-ray tube, electrons are produced by heating a filament (cathode) and accelerated towards a target (anode) by applying a voltage. If the incident electrons possess adequate energy, inner shell electrons of the target material will by knocked out. These electrons form the so-called characteristic X-rays, which are unique to the target material. For a diffraction structure analysis, additional filters are used to obtain monochromatic X-rays, which subsequently are focused and redirected towards the sample. The presence of only a singular wavelength with a known value is crucial to be able to identify the crystal structure from a diffraction pattern.

After creation, the rays are deflected in a sample as previously described in Bragg's law and the outcomes of these interactions are finally captured by the detector unit. While there are different kinds of detector operating principles, they all have in common that they, in simple terms, count the number of X-rays that are reflected at a certain angle as the measurement proceeds.

For examination of bulk materials, Bragg-Brentano XRD is commonly used, where the incident beam and reflected beam angle are both of the same value θ. Now, if the sample stands still, the X-ray source and detector need to move at the same angular velocity. While this is called a $\theta - \theta$ setup, if only the detector is tilting, it is called $\theta - 2\,\theta$ or grazing incidence principle.

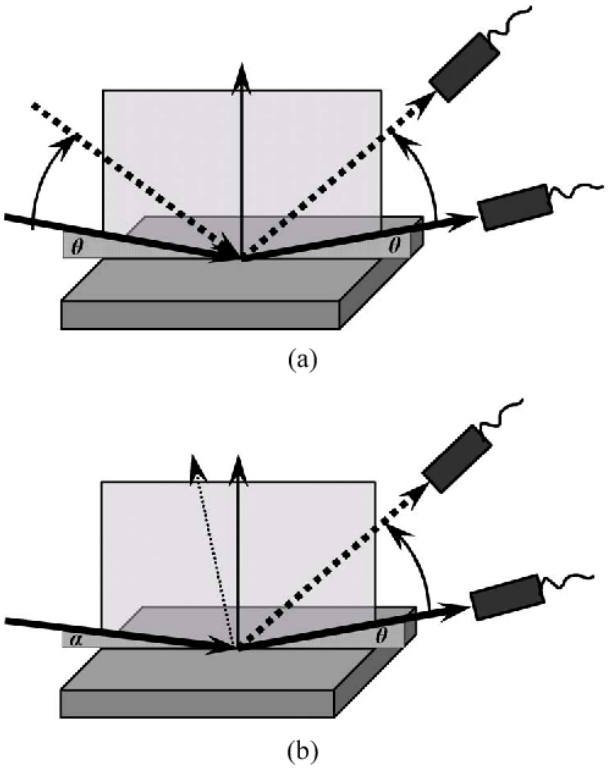

Fig. 11 Schematic illustration of (a) Bragg-Brentano and (b) grazing incidence diffractometers. Taken from [26].

For studying thin films or surface-near regions, especially the latter one is suited. In this arrangement the angle of the incoming X-ray beam is small, to have enough volume interaction while minimising the penetration depth of the beam. In an optimal situation for thin films penetration depth should be lower than the film thickness to avoid interfering signals from the substrate material. Otherwise, commonly the diffraction pattern of the used substrate is known and can be taken into account when conducting the graphical analysis of a diffractogram. The high volume interaction in a grazing incidence setup leads to loss in X-ray intensity which is why such measurement are usually more time consuming compared to Bragg-Brentano.

For the evaluation of a diffraction pattern, one must have a basic understanding of crystal lattices. To describe the atomic arrangement within a crystal, so-called Bravais lattices, named after its originator Auguste Bravais, are commonly used. The basic idea of this approach is to describe a crystal lattice by specifying its smallest possible repeating segments, the so-called unit cells. For it to be classified as a Bravais lattice every point in the arrangement must have the same surroundings in a geometrical and atomistic way. In a

three-dimensional space there are 14 different Bravais lattices with their related unit cells sufficient to describe every possible lattice arrangement (see Fig. 12). Every unit cell is defined by three translational vectors along with six lattice parameters, the lengths of the three cell edges and their relative angles. Through translational operations these cells form a periodic crystal lattice.

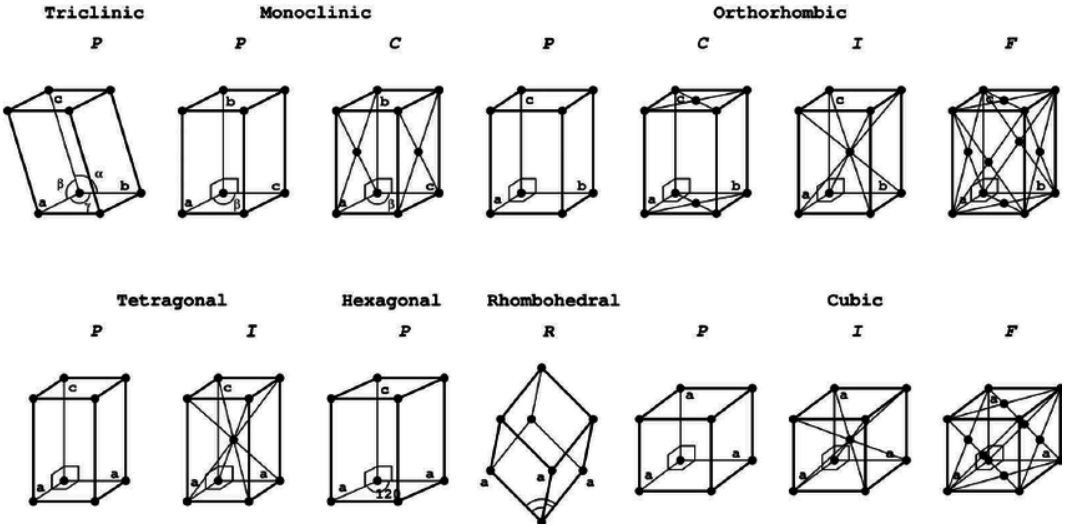

Fig. 12 The 14 Bravais lattices. Taken from [27].

To designate certain crystallographic planes in a lattice, at which the X-ray diffraction may occur, a notation system based on the Miller indices is employed. This system is capable to denote families of parallel planes in a periodic crystal lattice. The indices h, k and l represent the reciprocal values of the interceptions between a plane and the three crystal axes. In other words, the indices represent a normal vector to a certain family of parallel planes. In an example calculation of a lattice plane in a simple cubic system is shown.

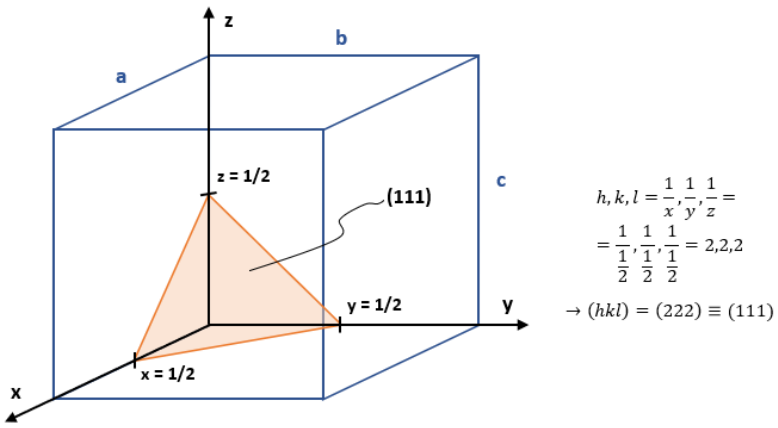

Fig. 13 Calculation of the Miller indices for a plane in a simple cubic unit cell (own work).

Commonly, the shortest possible reciprocal lattice vector is used to describe a group of equivalent planes. Thus, the calculated (222) plane in Fig. 13 is equivalent to the (111) plane.

In Fig. 14 two diffractometer measurements of dissimilar thin film coatings are displayed. The general positions of the peaks suggest that the present lattice is of a cubic nature. By knowledge of the peak diffraction angles, the lattice constants can easily be calculated.

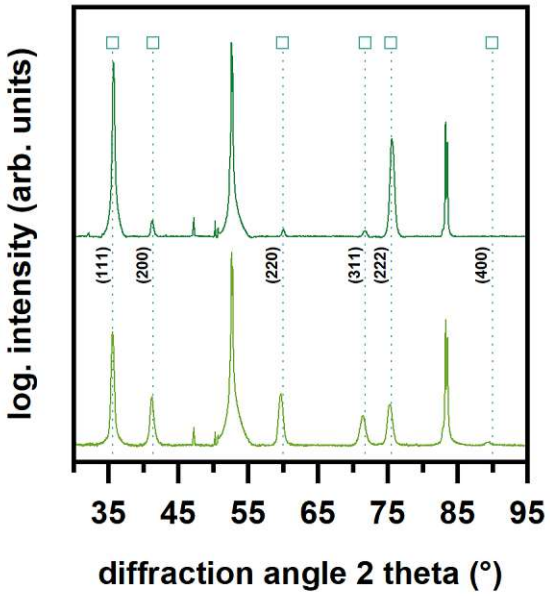

Fig. 14 Preferred growth direction demonstrated by XRD Patterns of to different cubic samples (own work).

The peaks of both samples align quite well, yet there is a notable difference in their intensities. The upper pattern has a strong manifestation in the (111) direction and its relatives which states that this is the preferred growth direction in the sample's crystal lattice.

The dotted vertical lines, as plotted in Fig. 14, are a common practice to compare a measured pattern with a reference pattern of a known substance to be able to draw conclusions about the crystal structure and even chemical composition of a sample. In this example, a cubic refence pattern was overlayed. The peaks, which do not align with the reference can be assigned to the substrate material, whose diffraction pattern is known.

This is just a simple example of a XRD pattern analysis. There can occur many other phenomena which provide insight about grain sizes or residual stresses in a crystal lattice.

6.2 Indentation testing

Perhaps the most common way to determine the mechanical properties of materials are indentation hardness testing methods like Vickers or Rockwell for example, where a standardised indenter is pushed into to surface of the sample material with a predefined force. Then, commonly by optically measuring the depth or size of the indentation and by knowledge of the applied maximum force, the hardness of the sample can be calculated. The hardness is generally a measure to describe the resistance of a surface to indentation. Furthermore, there are also models to calculate the elastic modulus of a specimen by indentation tests.

Within this thesis thin films with thicknesses in the low micrometre-range were tested. The indentation depth of conventional macro indentation test methods would exceed the existing film thicknesses. A general rule for testing thin films is that the indentation depth should not be more than ten percent of the overall thickness of the film, to avoid influences of the substrate material [28]. As mentioned before, thin film thicknesses are normally in or even below the micrometre range. To still be able to quantify the characteristics of such small volumes of material, nanoindentation is used.

6.2.1 Nanoindentation testing

In nanoindentation-testing, as the name already suggests, very small tip sizes and indentation loads are used. The result of such tests are indentation marks in the range of square micrometres or even nanometres. To be able to quantify such marks, scanning electron microscopy would constitute a suitable method. As this would be a quite tedious task, a different approach is taken.

In nanoindentation testing, a high precision diamond tip (usually a three-sided Berkovich tip, see Fig. 15) with known geometry is applied and the depth of penetration along with the applied force is recorded over the course of the process. By the knowledge of this data, the size of the indentation can be calculated and with this also the hardness and elastic modulus of the material. For this it is particularly vital to exactly determine the initial contact between the indenter and sample surface at the beginning of each measurement, as it constitutes the zero point for the displacement value [28].

As one could possibly imagine, a very precise knowledge of the tip geometry is essential to obtain realistic measurement results. Furthermore, to account for the decreased sharpness of the tip after a certain period of usage, a so-called area function must be recorded and subsequently included in the evaluation of the measured data. Apart from its geometry, also the stiffness of the tip and the remainder of the measurement apparatus must be accounted for.

Besides calibration of the measurement device, there are a few other sources of error in nanoindentation measurements. It is essential to avoid mechanical vibrations and thermal variations in the direct surroundings of the indenter. Also, slight errors in the sample preparation can lead to meaningless results.

Lastly, the film properties can have a strong influence on the quality of the measurement results. Besides the general ten percent rule concerning the film thickness, a smooth and failure-free surface is key.

During the measurement, a common phenomenon is a pile-up of sample material at the borders of the indentation mark, which leads to an enlargement of the contact surface and further an overestimation of the hardness value. On the contrary, sinking in of sample material is possible which generates the opposite effect. As these effects can hardly be corrected for, they are usually ignored. If this is the case, the results of a nanoindentation measurement can only be viewed as comparative values to be precise [28].

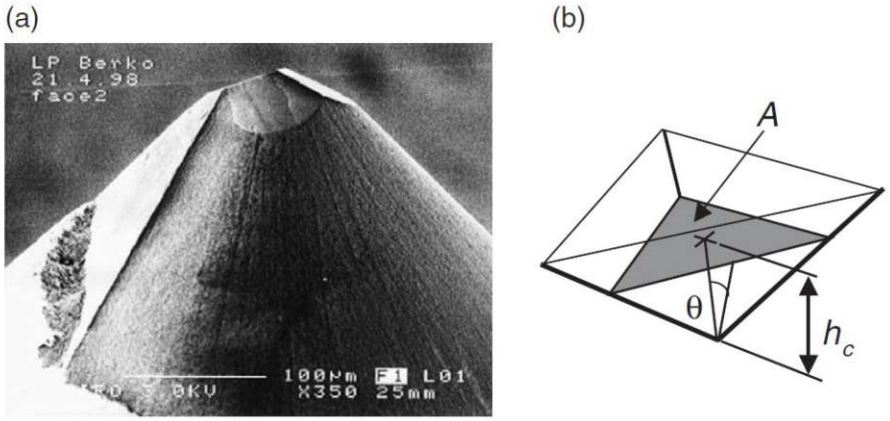

Fig. 15 (a) SEM image of a Berkovich indenter tip and (b) schematic of the tip geometry, where θ (=65.27°) is the face half-angle, A is the projected contact area and $\boldsymbol{h_c}$ is the contact depth. Taken from [28].

As mentioned before, besides the indentation depth, the penetration load is measured. This data can be used to create load-displacement curves which allow to make statements about the mechanical properties of the test piece (see Fig. 16).

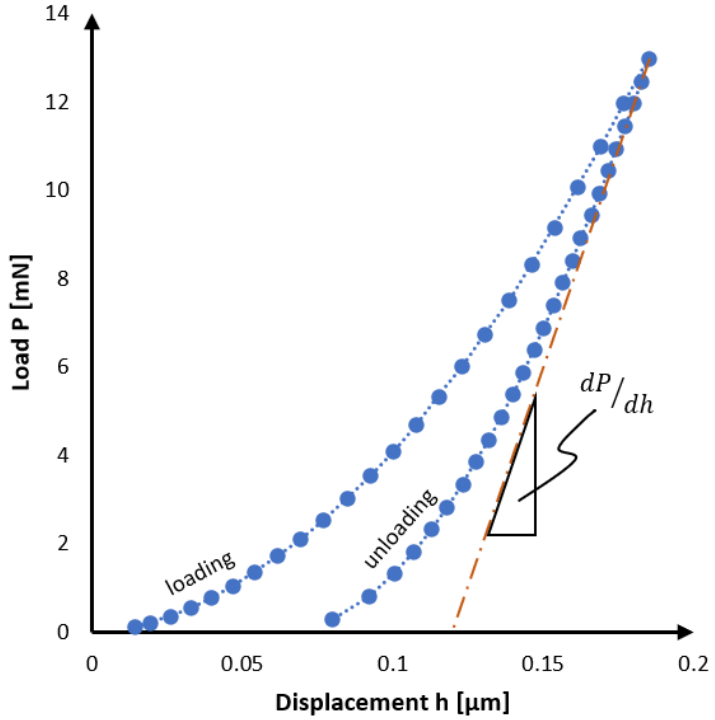

Fig. 16 Exemplary load-displacement curve of an indentation test (own work).

For example, the slope $^{dP}/_{dh}$ at the beginning of the unloading-curve, also called contact stiffness, in combination with the projected area of contact can be used to quantify the combined modulus of elasticity of.

By recording a series of indentation tests with a range of test forces, or rather penetration depths, and subsequently fitting a curve to the plotted results, a value for the elastic modulus can be obtained by extrapolating to a penetration depth of zero [28] (see Fig. 17). This is quite significant for thin films as it is impossible to evaluate their modulus with traditional tensile testing methods.

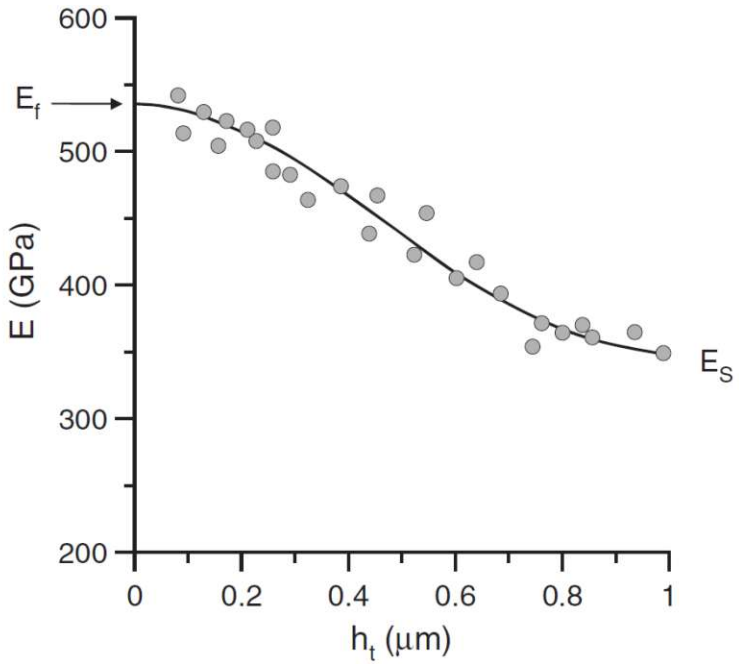

Fig. 17 Estimation of the elastic modulus of a testing series by extrapolation to zero penetration depth, taken form [28].

To reinforce the results of the conducted hardness tests, several indentations on the same sample should be carried out. Obviously, this requires a uniform surface finish without imperfections at least in the tested area. If required, the surface can be polished before the measurement. Finally, for both hardness and modulus of elasticity of the film, a mean value is calculated from the measurement series. To make statements about the accuracy of the conducted test, the standard deviation of the collected data should be reviewed.

6.3 Scanning electron microscopy

In scanning electron microscopy, or in short, SEM, the interactions between a finely focused beam of electrons and the atoms in a sample are analysed to obtain information about surface topography or even composition of the examined specimen. By guiding the electron beam over a surface in a raster-like manner and analysing the response of the sample at each point, information concerning the external morphology, chemistry and even crystal structure can be imaged with a variety of different signal detectors. To avoid distractions from the atmosphere, specimens are examined under vacuum and resolutions up to the nanometre range can be achieved.

As the electron beam impinges it dissipates energy in a teardrop shaped portion of the specimen (see Fig. 18). Consequentially, through interactions with the atoms inside this volume certain electrons are scattered or ejected and able to leave the sample to be captured by the appropriate detector unit [23].

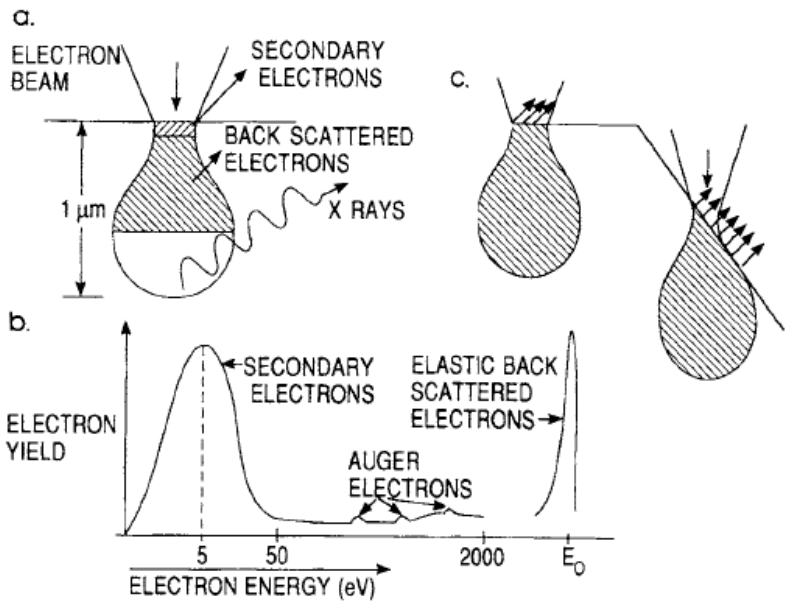

Fig. 18 (a) Teardrop-shaped interaction volume, (b) emitted electron energy spectrum and (c) topographic effects on electron emission. Taken from [23].

For the majority of the SEM-imaging operations a secondary electron or a backscattered electron detector is used. While secondary electrons originate only from the first few angstroms from the surface, the high-energy backscattered electrons are able to travel larger distances inside the sample (see Fig. 18a).

Secondary electrons are typically low in energy (see Fig. 18b) which implies that they are only able to escape the sample if they are created in the near surface region. As shown in Fig. 18 (c), the surface portion under interaction is depending on the relative orientation to the beam direction. Because of this behaviour, secondary electrons are preferably utilised to examine the surface topography of specimens.

The topography contrast of backscattered electron images is much weaker compared to the secondary-electron-based detection as they interact with a much large volume of the sample. To put it simply, the trajectory of incident electrons is gradually changed as they are attracted to the atom cores in the sample. Eventually, after a sufficient number of scattering events some of these electrons will finally be scattered back out of the sample. Backscatter electron imaging is primarily useful to display variations in the composition or different phases, as the efficiency of the electron redirection largely depends on the atomic number of the substance under investigation [23].

6.3.1 Energy-dispersive X-ray spectroscopy

With an energy dispersive X-ray detector, or in short, EDX, information about the chemical composition of a sample as well as the element distribution can be generated. Commonly such measurements are conducted inside a SEM, where the electron beam is used to excite the sample. The principle is based on the emission of characteristic X-rays resulting from electrons hitting the inner shells of the atoms. The energy of this X-rays is unique to each element. An EDX detector converts this characteristic energy into electric voltage and the received signals are displayed using a suitable software in a spectrum as shown in Fig. 19.

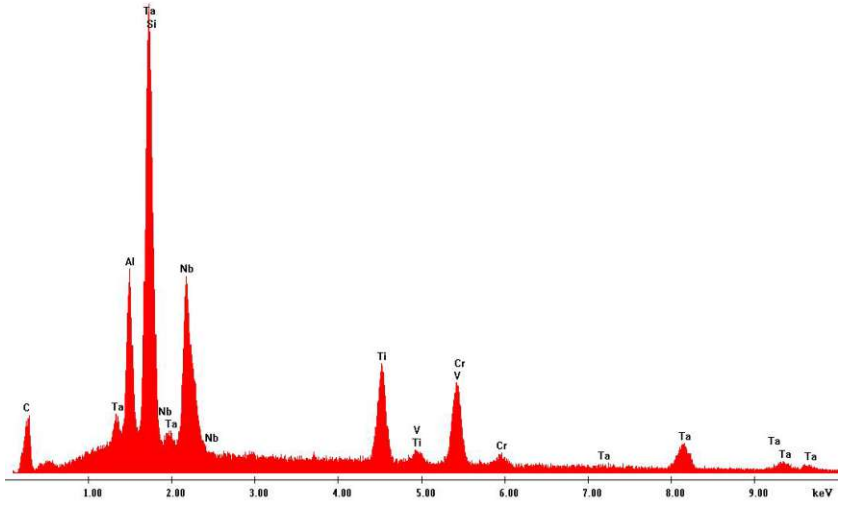

Fig. 19 Example EDX spectrum of a high-entropy carbide thin film (own work).

In principle, the counts of electric pulses at a certain energy level correspond to the element concentration in the sample. Based on this an evaluation software is then able to provide information about the atomic percentages of the elements in a sample material.

A common problem in X-ray spectroscopy is the overlapping of peaks of different elements, which makes the evaluation difficult. If the characteristic radiation energies of two elements present in the examined sample are diverging by a lower value than the measurement resolution, the spectrum peaks can likely not be analysed correctly. In Fig. 19 for example, the silicon K-emission peak is swallowed by the tantalum M-emission peak. Therefore, the resulting measurement values for those two elements should be viewed with distrust.

If X-rays are utilised to excite the sample, the process is usually referred to as X-ray fluorescence spectroscopy (XRF) and performed in a standalone instrument. Due to the higher energy of the X-rays compared to the electron beam in a SEM-EDX, this measurement setup theoretically favours the heavier elements.

7 Results and Discussion

All depositions in the frame of this work were performed with the PVD system displayed in Fig. 20 by using a equimolar metallic 3 inch AlCrNbTaTi target on at least one sapphire, silicon and austenite substrate (see Fig. 21) to be able to conduct all of the wanted investigations. Before installing them in the deposition chamber they were ultrasonically cleaned in acetone and ethanol for several minutes. After reaching a background pressure below 0.5 mPa at the desired substrate temperature they were etched for 10 minutes with Ar-ions by applying a -800 V DC Bias at a gas pressure of around 4.9 Pa. Directly after etching, the deposition process was started. The distance between the sputtering target and the substrates was set to 70 mm and slight rotation was applied to the substrates to increase the uniformity of the films. The total gas flow during all depositions was set to 20 sccm resulting in a gas pressure of around 0.32 Pa while the ratio between reactive acetylene and inert argon gas was altered between some coatings. The sputtering was conducted in DC mode at a power density in the range of 7 to 9.5 W/cm^2 while -50 V DC Bias was applied.

Fig. 20 Lab-scale PVD system capable of depositing carbides by reactive magnetron sputtering with acetylene ($\mathbf{C_2H_2}$) gas.

As a starting point, a deposition run with reactive acetylene gas ratios of 10 %, 20 % and 30 % was carried out at a substrate temperature of 450 °C.

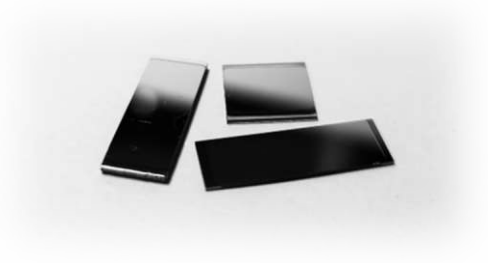

Fig. 21 Thin film samples on sapphire, silicon and austenite substrates prepared by reactive magnetron sputtering.

The XRD patterns of the resulting films are displayed in Fig. 22. These diffractograms clearly indicate that an acetylene flow rate of 20 % promotes the formation of a desirable cubic solid solution phase with a cell parameter of 4.380 Å while at 10 % as well as 30 % a largely amorphous structure is formed. All of the XRD measurements in this work were undertaken by a X'Pert MDPII Bragg-Brentano diffractometer with a $Cu_{K\alpha}$ radiation source.

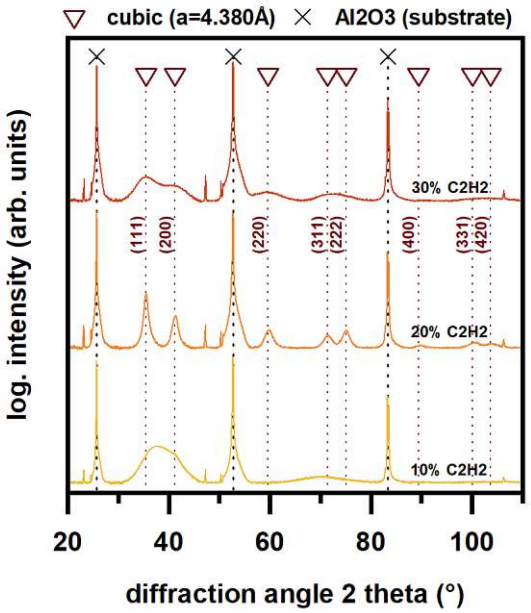

Fig. 22 X-ray diffraction patterns of AlCrNbTaTi carbide thin films deposited with reactive gas ratios of 10 %, 20 % and 30 % at a substrate temperature of 450 °C. Reference data for a cubic phase with a lattice constant of 4.380 Å (red triangles) as well as the $\mathbf{Al_2O_3}$ substrate (black crosses) is indicated.

Based on the findings of these initial depositions, additional films were synthesised using a reactive gas flow rate of 20 % at substrate temperatures of 550 °C and 650 °C. As displayed in Fig. 23 a cubic lattice is dominant for all temperature levels, yet the slight broadening of the peaks at 650 °C could suggest the presence of finer grains compared to the lower temperature levels. Concerning the peak intensities, the three depositions show a preferred growth towards the (111) direction while this manifestation is most pronounced at 550 °C.

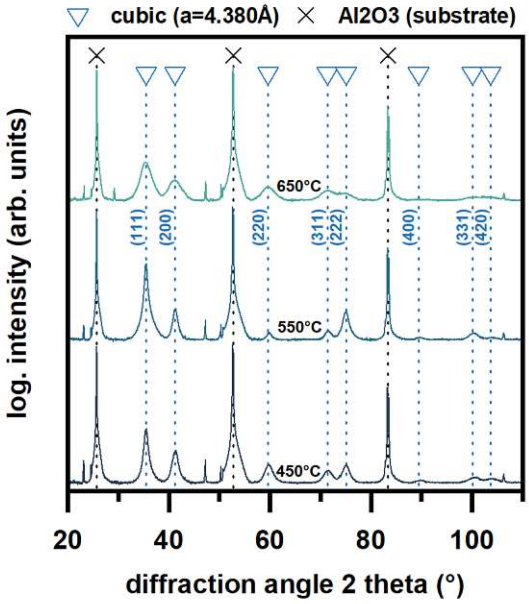

Fig. 23 X-ray diffraction patterns of AlCrNbTaTi carbide thin films deposited with substrate temperatures of 450 °C, 550 °C and 650 °C at a reactive gas ratio of 20 %. Reference data for a cubic phase with a lattice constant of 4.380 Å (light blue triangles) as well as the $\mathbf{Al_2O_3}$ substrate (black crosses) is indicated.

Taking the established favourable deposition parameters, a series of depositions to investigate the influence of adding different portions of silicon to the alloy was conducted. This has previously been shown to be beneficial for the hardness, high temperature stability and especially oxidation behaviour of nitride thin films based on the same alloying system [7]. As the composition of the sputtering target is not easily changeable or rather the manufacturing of a new target would be expensive, the alloying was done by placing small evenly sized silicon platelets on the target racetrack as illustrated in Fig. 24.

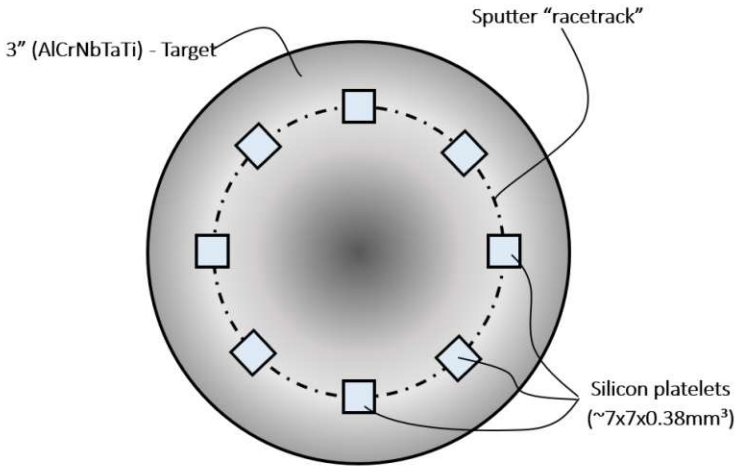

Fig. 24 Schematic illustration of the silicon platelets placement on the sputtering target.

To find out how much of the silicon made its way into the films during the synthesis, top-view SEM-EDX measurements were carried out. The results of these experiments are displayed in Fig. 25 and Tab. 1.

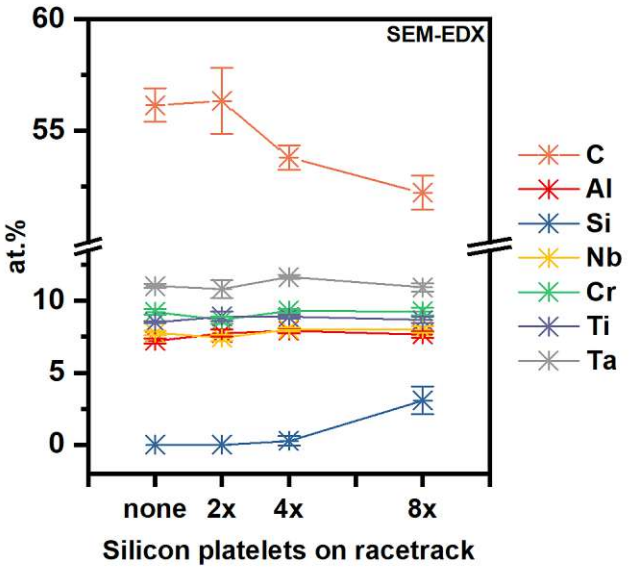

Fig. 25 Chemical composition of the silicon alloyed AlCrNbTaTi carbides depending on the number of silicon platelets placed on the sputter racetrack, obtained by top-view SEM-EDX.

	Chemical composition (at%)			
	no Si	2xSi	4xSi	8xSi
C	56.15±0.74	56.33±1.48	53.8±0.56	52.24±0.76
Si	-	0	0.27±0.34	3.08±0.96
Al	7.12±0.18	7.75±0.24	7.94±0.17	7.66±0.22
Nb	7.77±0.17	7.43±0.2	8.02±0.12	7.99±0.23
Ti	8.51±0.07	8.9±0.33	8.89±0.13	8.67±0.21
Cr	9.22±0.2	8.66±0.26	9.3±0.11	9.26±0.25
Ta	11.03±0.11	10.82±0.64	11.64±0.13	10.93±0.28

Tab. 1 Chemical composition of the silicon alloyed AlCrNbTaTi carbides depending on the number of silicon platelets placed on the sputter racetrack, obtained top-view SEM-EDX.

Taking a closer look at these results, it is conspicuous that no silicon was detected in the second sample while also the error bar for the tantalum value is large in comparison to the other samples. So, it can be concluded that there is some form of issue with the measurement. When looking at the recorded EDX spectrum it becomes clear why this error occurs. The silicon K-shell and the tantalum M-shell peaks are too close to each other to be clearly distinguished by the analysis software (see Fig. 19). The used EDAX spectrometer is capable of resolutions down to 130 eV while the spacing between the mentioned peaks would theoretically be 30 eV. For tantalum also the L-shell emission peak was quantified to improve the accuracy of the measurements, but the resulting silicon values should be treated with caution.

To get a second view on the chemical composition of the samples, X-ray fluorescence was deployed. Unfortunately, with the used Omnian XRF analysis software it was not possible to quantify the carbon content of the samples. Thus, the percentages displayed in Fig. 26 correspond only to the whole of metallic elements in the samples.

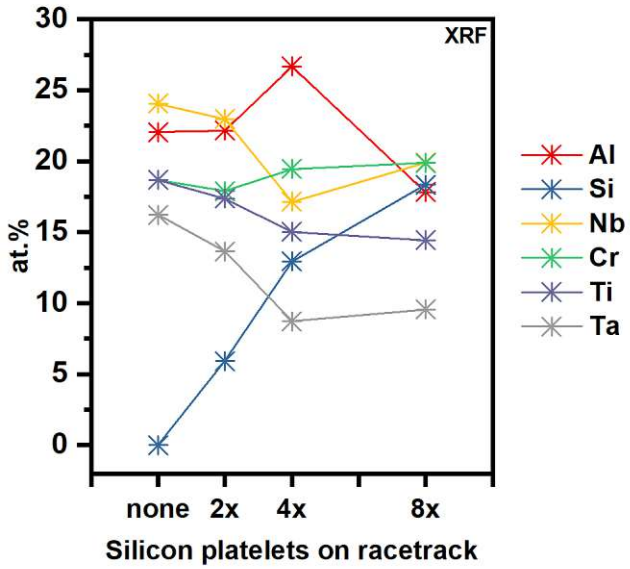

Fig. 26 Chemical composition of only the metallic elements of the silicon alloyed AlCrNbTaTi carbides depending on the number of silicon platelets placed on the sputter racetrack, obtained by XRF.

The comparably high aluminium as well as the low tantalum contents, especially for the sample sputtered with four silicon platelets, do not agree with the EDX results. They should be much closer to the values of the other target elements as it is composed equimolar. The underestimated percentage is presumably connected to the fact that the high energetic L-shell emission line was used for the analysis of the tantalum which is expected to be far from fully absorbed at a present film thickness of around 4 µm. Based on the consideration of shell emission energies, the aluminium content should be the least underestimated which would explain the elevated values. Unfortunately, it was not possible to quantify the lower energy tantalum M-shell emission line with the available equipment, which would improve the accuracy of the measured values. Nevertheless, the silicon contents attained by this XRF analysis should not deviate too much and will be used to denote the different samples in the following paragraphs.

Considering the elemental composition of the metallics attained by XRF and including in the carbon values from the EDX analysis leads to the elemental distribution displayed in Fig. 27 as well as Tab. 2.

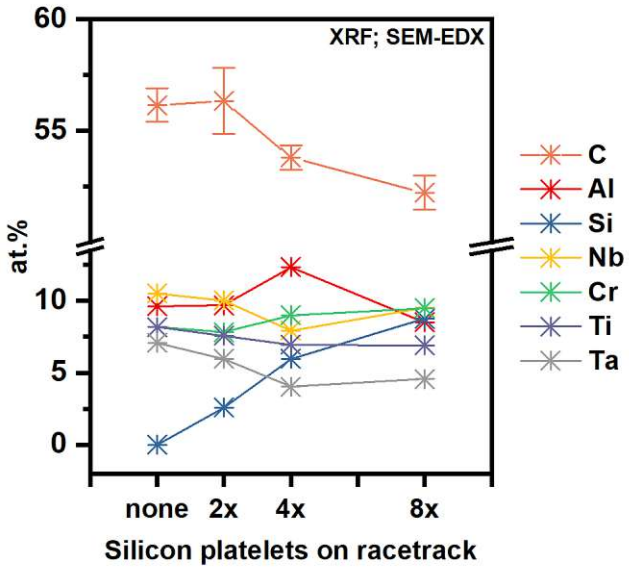

Fig. 27 Chemical composition of the silicon alloyed AlCrNbTaTi carbides depending on the number of silicon platelets placed on the sputter racetrack, obtained by X-ray fluorescence and top-view SEM-EDX.

	Chemical composition (at%)			
	no Si	2xSi	4xSi	8xSi
C	56.15	56.33	53.8	52.24
Si	-	2.59	5.98	8.76
Al	9.63	9.68	12.33	8.76
Nb	10.52	10.03	7.92	9.51
Ti	8.17	7.58	6.94	9.6
Cr	8.17	7.82	8.99	9.49
Ta	7.09	5.96	4.03	4.57

Tab. 2 Chemical composition of the silicon alloyed AlCrNbTaTi carbides depending on the number of silicon platelets placed on the sputter racetrack, obtained by XRF (metals) and top-view SEM-EDX (carbon).

The effects of alloying silicon to the HECs on their lattice can be seen in Fig. 28. The XRD diffractograms show that generally the same cubic phase can be observed independent of the silicon content. There is in principle no difference between the lowest alloyed and the sample without any silicon in the compound. At higher silicon contents shifts in the peak intensities, which implies a change in the preferred growth direction, can be observed. The preferred growth shifts from a strong (111) orientation to a clear (200) orientation for the highest alloyed sample.

Additionally, upon closer examination there is a very slight shift of the peaks to smaller angles for the highest alloyed sample. Taking Braggs Law into account this could mean that the lattice spacing is increasing slightly with silicon content. Additionally, at least the sample containing 8.76 at.% silicon shows a broadening of the peaks which usually is attributed to a refinement of the grains.

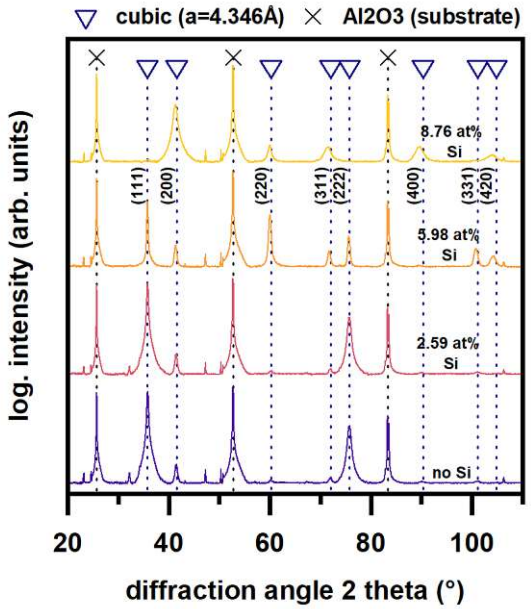

Fig. 28 X-ray diffraction patterns of silicon alloyed AlCrNbTaTi carbide thin films deposited with a substrate temperature of 550 °C at a reactive gas ratio of 20 %. Reference data for a cubic phase with a lattice constant of 4.346 Å (blue triangles) as well as the $\mathbf{Al_2O_3}$ substrate (black crosses) is indicated.

As displayed in Fig. 29, the addition of silicon causes a slight decrease in the film growth rate from 108 nm/min for no silicon addition to 94 nm/min for the 8.76 at.% silicon sample. The SEM cross-sections also confirm the suspicion that an increasing silicon content leads to refinement of the grain changing from a coarser structure in Fig. 29a to a rather featureless structure in Fig. 29d.

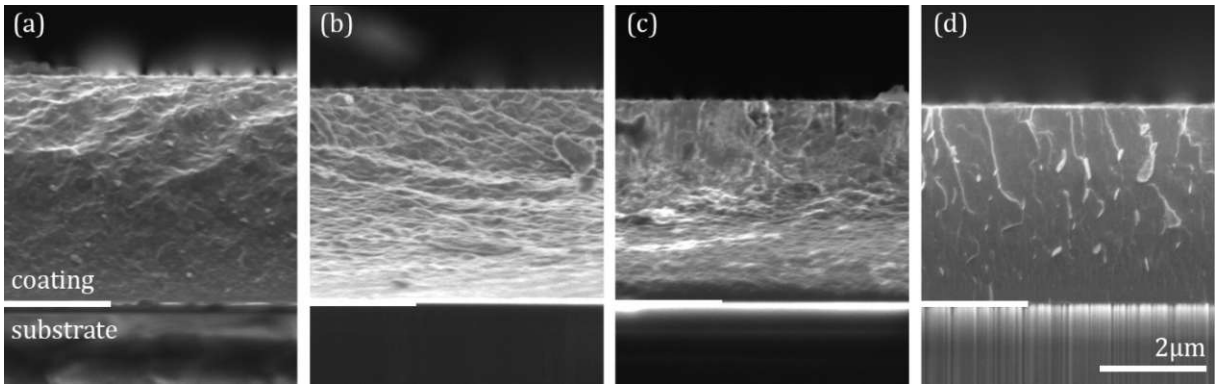

Fig. 29 SEM fracture cross-sections of AlCrNbTaTi carbide thin films with different amounts of additional silicon deposited on sapphire. With (a) no, (b) 2.59 at.%, (c) 5.98 at.% and (d) 8.76 at.% silicon.

Concerning the mechanical properties of the HEC thin films (see Fig. 30; Tab. 3), only a slight impact from silicon addition can be observed. The hardness increases from 28.8 GPa to 30.3 GPa for the maximum silicon content while the indentation modulus undergoes a rise from 413 GPa to 449 GPa. When considering the error bars of these measurements, these increases are rather insignificant.

The only irregularity can be noted for the sample containing 2.59 at.% silicon. The indentation modulus is decreased to 378 GPa for this sample which could theoretically point to an increased performance in terms of toughness and wear.

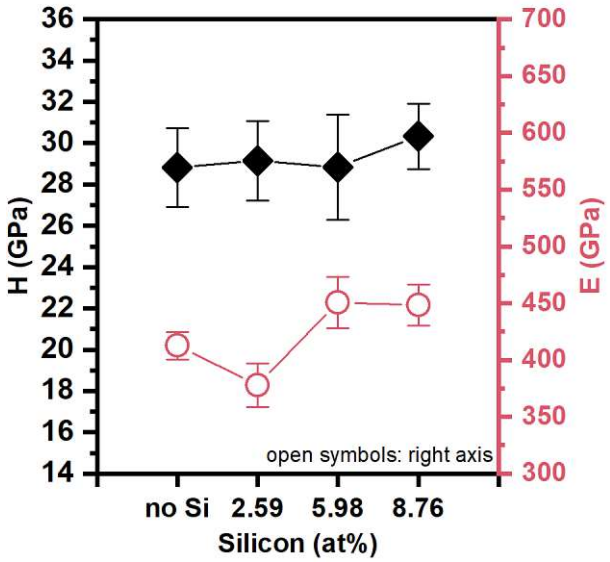

Fig. 30 Hardness values and indentation moduli of the AlCrNbTaTi carbide thin films depending on the silicon content obtained by nanoindentation.

	Mechanical properties			
Si (at%)	-	2.59	5.98	8.76
H (GPa)	28.8 ± 1.9	29.2 ± 1.9	28.8 ± 2.5	30.3 ± 1.6
E (GPa)	413 ± 12	378 ± 19	451 ± 23	449 ± 18

Tab. 3 Mechanical properties of the AlCrNbTaTi carbide thin films depending on the silicon content obtained by nanoindentation.

Vacuum annealing treatments were carried out at temperatures of 800 °C, 900 °C and 1000 °C. The annealing cycle for each temperature was pre-programmed to a heating rate of 20 K/min and the target temperature was held for 10 minutes before the samples were left to cool down passively in the vacuum. The same experiments were done for all samples, thus only the ones containing 8.76 at% silicon were able to endure all temperature levels. For the 5.98 at% silicon samples the limit was at 800 °C while the remaining films did not even survive this temperature level. Among other factors, this could also be connected to a large mismatch of the thermal expansion coefficient between film and substrate as the surviving samples consistently showed cracks.

Looking at the resulting XRD data in Fig. 31 as well as Fig. 32 the vacuum annealing treatments seem to have no impact on the structure of the films as there are no substantial differences visible between the patterns.

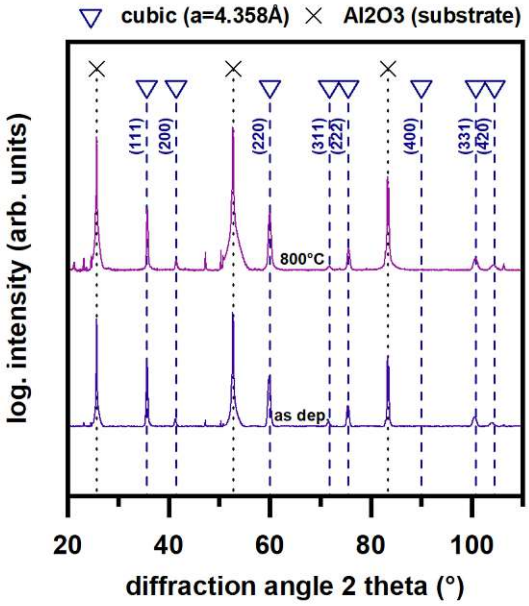

Fig. 31 X-ray diffraction patterns of silicon alloyed AlCrNbTaTi carbide thin films in the as deposited state as well as vacuum annealed at 800 °C for 10 minutes. Reference data for a cubic phase with a lattice constant of 4.358 Å (blue triangles) as well as the $\mathbf{Al_2O_3}$ substrate (black crosses) is indicated.

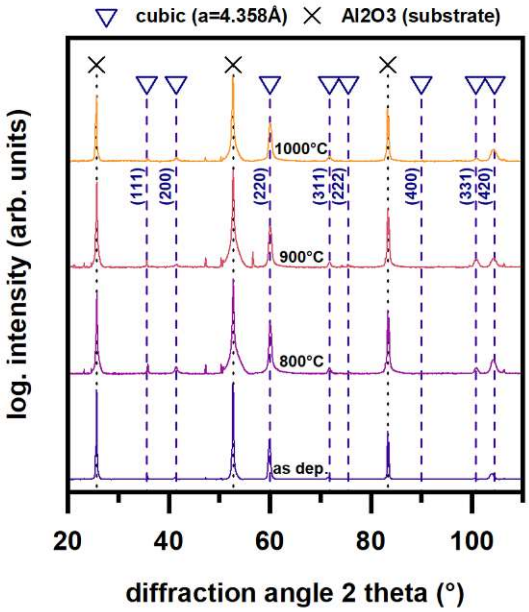

Fig. 32 X-ray diffraction patterns of silicon alloyed AlCrNbTaTi carbide thin films in the as deposited state as well as vacuum annealed at 800 °C, 900 °C and 1000 °C for 10 minutes. Reference data for a cubic phase with a lattice constant of 4.358 Å (blue triangles) as well as the $\mathbf{Al_2O_3}$ substrate (black crosses) is indicated.

Concerning the mechanical properties (see Tab. 4), the harness values remain more or less unaffected by the vacuum annealing for both samples. At 5.98 at.% silicon the films show a slight increase in the indentation modulus while the ones at 8.76 at.% undergo a decrease of the indentation modulus the higher the annealing temperature. This could, as explained previously, point to an increased toughness and decreased wear rate for some applications.

The decreasing modulus values can most likely be connected to recovery and recrystallisation processes occurring due to the thermal activation. Through this, internal stresses and growth defects arising from the synthesis of the films can be to some extent be annealed out. Theoretically, if internal compressive stresses are diminished, the hardness of the film should decrease, which cannot be observed here. The unchanged values may be connected to the introduction of compressive stresses during the cooling of the samples, if the substrates possess a greater coefficient of thermal expansion compared to the films. The reduction of hardness due to recovery processes could then be counteracted by these internal stresses. Unfortunately, the available data on thermal expansion of HECs is still very limited. Further investigations would be necessary to support or rebut this hypothesis.

Mechanical properties

Si (at%)	5.98		8.76			
T (°C)	as dep.	800	as dep.	800	900	1000
H (GPa)	28.8 ± 2.5	29.8 ± 2.9	30.3 ± 1.6	29.5 ± 1.3	29.7 ± 1	29.3 ± 0.9
E (GPa)	451 ± 23	481 ± 31	449 ± 18	407 ± 17	381 ± 13	375 ± 14

Tab. 4 Mechanical properties of the vacuum annealed silicon alloyed AlCrNbTaTi carbide thin films depending on the annealing temperature obtained by nanoindentation.

The oxidation behaviour of the silicon alloyed AlCrNbTaTi carbide thin films was investigated through ambient air annealing treatments at temperatures of 600 °C, 700 °C and 800 °C for time periods of 1 h, 5 h as well as 10 h. The chamber furnace was preheated to the target temperature before the samples were put in.

As a starting point the sample without silicon addition was annealed in ambient air at a temperature of 600 °C. Concerning the XRD data in Fig. 33 no significant change between the diffractograms, or to put it differently, no emergence of an oxide phase, is visible.

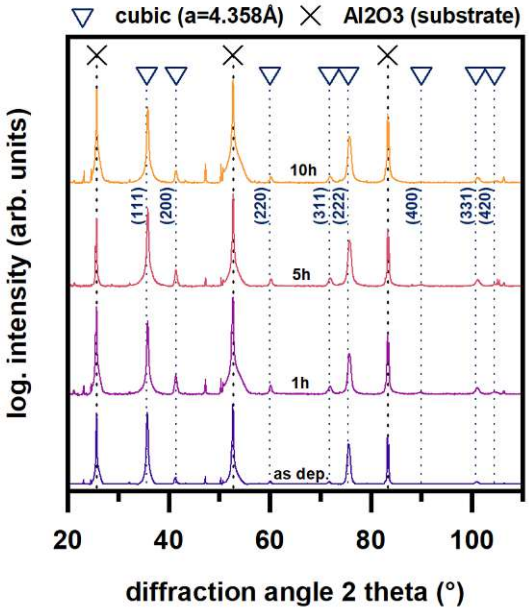

Fig. 33 X-ray diffraction patterns of AlCrNbTaTi carbide thin films in the as deposited state as well as oxidised at 600 °C for 1 h, 5 h, and 10 h. Reference data for a cubic phase with a lattice constant of 4.358 Å (blue triangles) as well as the $\mathbf{Al_2O_3}$ substrate (black crosses) is indicated.

Under examination of the fracture cross sections displayed in Fig. 34, a visible oxide scale with a thickness of roughly 190 nm is forming after 5 h which is increasing to 320 nm after 10 h.

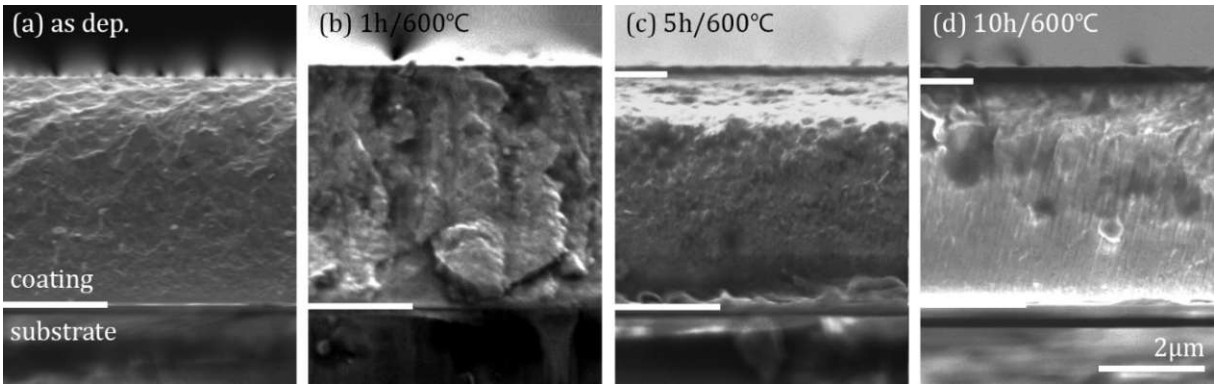

Fig. 34 SEM fracture cross-sections of AlCrNbTaTi carbide thin films on sapphire substrates in the (a) as deposited state as well as oxidised at 600 °C for (b) 1 h, (c) 5 h and (d) 10 h.

At an oxidation temperature of 700 °C the first clear oxide phase peaks are emerging in the XRD pattern (see Fig. 35) after 5 h and intensifying after 10 h of annealing. The forming oxide scale possesses a rutile-like tetragonal crystal structure. This aligns with oxidation

studies on AlCrNbTaTi nitride films which also formed a rutile-type oxide scale at ambient air annealing [7]. Additionally, research has been performed on reactively sputtered oxide films of the same base material system which possess a single-phase rutile-like structure [6].

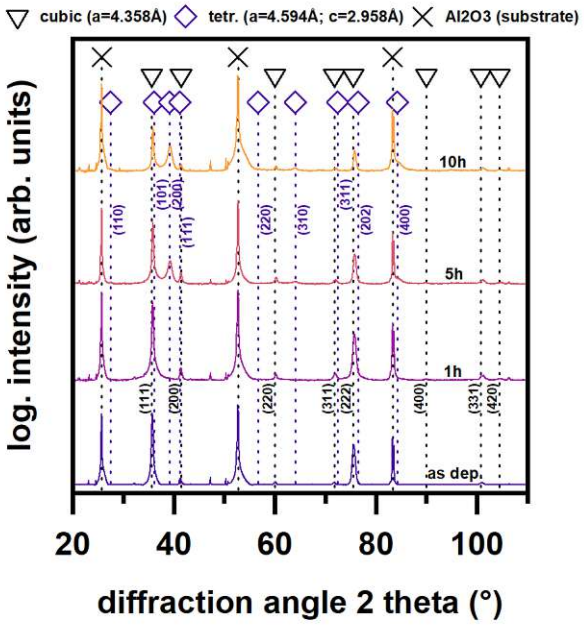

Fig. 35 X-ray diffraction patterns of AlCrNbTaTi carbide thin films in the as deposited state as well as oxidised at 700 °C for 1 h, 5 h, and 10 h. Reference data for a cubic phase (black triangles), a tetragonal oxide phase (blue cubes) as well as the $\mathbf{Al_2O_3}$ substrate (black crosses) is indicated.

As displayed in Fig. 36, the oxide scale is already clearly visible after 1 h of annealing with a thickness of 450 nm. The scale further thickens to 1.9 µm after 5 h and 3.7 µm after 10 h of oxidation. Along with the increase in oxide scale thickness, the remaining carbide film thickness is decreasing from initially 4.3 µm after 1 h to 3.7 µm and 2.8 µm after 5 h and 10 h.

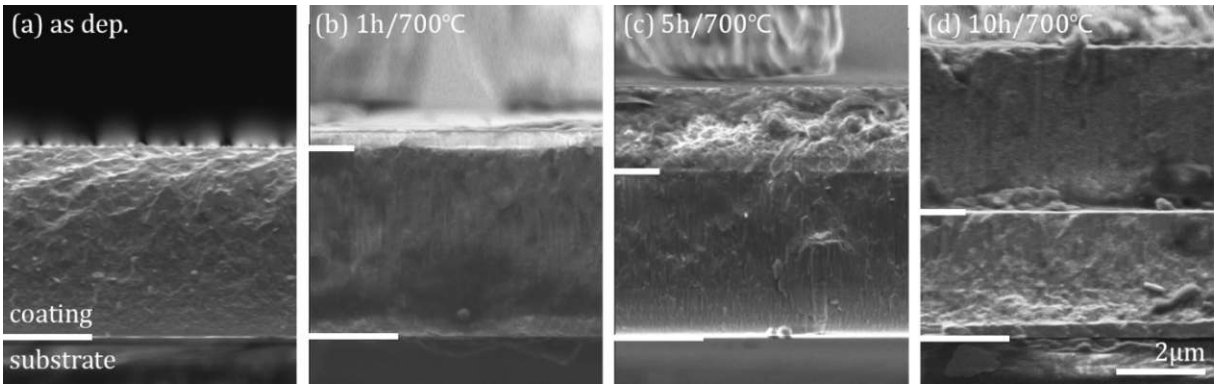

Fig. 36 SEM fracture cross-sections of AlCrNbTaTi carbide thin films on sapphire substrates in the (a) as deposited state as well as oxidised at 700 °C for (b) 1 h, (c) 5 h and (d) 10 h.

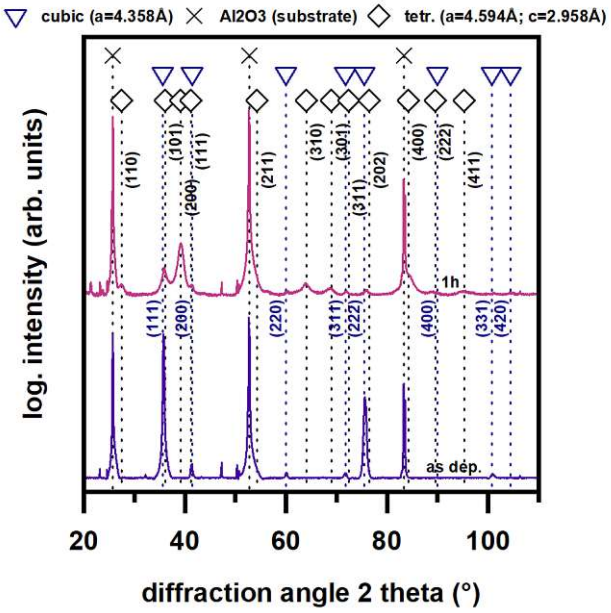

Fig. 37 X-ray diffraction patterns of AlCrNbTaTi carbide thin films in the as deposited state as well as oxidised at 800 °C for 1 h. Reference data for a cubic phase (blue triangles), a tetragonal oxide phase (black cubes) as well as the $\mathbf{Al_2O_3}$ substrate (black crosses) is indicated.

At an annealing temperature of 800 °C the oxide growth is much stronger compared to the lower temperature levels. After just 1 h the oxide has risen to a thickness of a 7.8 µm with a remaining carbide film thickness of 770 nm, as pictured in Fig. 38.

The XRD patterns displayed in Fig. 37 after 1 h of treatment presumably mostly consists of the rutile-structured oxide peaks with only a few cubic carbide peaks left.

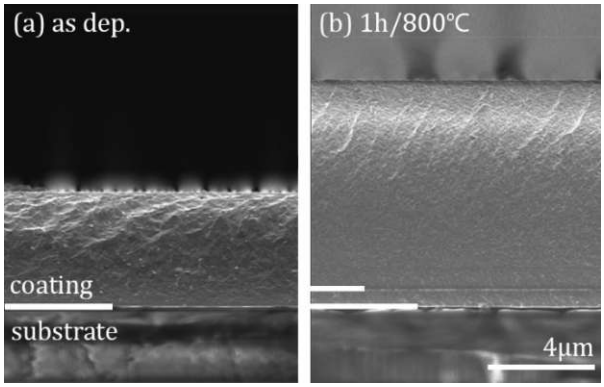

Fig. 38 SEM fracture cross-sections of AlCrNbTaTi carbide thin films on sapphire substrates in the (a) as deposited state as well as oxidised at 800 °C for (b) 1 h.

Looking at the sample after the treatment, this seems to be on the limits of the capabilities of this film as its borders already started to peel off from the substrate slightly. After 5 h of annealing more or less only the sapphire was left after the film detached from the substrate. Thus, it can be concluded that the oxide scale increases the temperature stability of the film as it was not capable of enduring the vacuum annealing at 800 °C for 10 minutes.

The addition of silicon to the composition of the high-entropy carbide films clearly impedes the oxide growth. The 2.59 at.% silicon sample showed no new peaks even after 5 h at 700 °C, though it is possible that there are rutile-structured oxide peaks which align with the cubic structure of the underlaying carbide film, as indicated in Fig. 39.

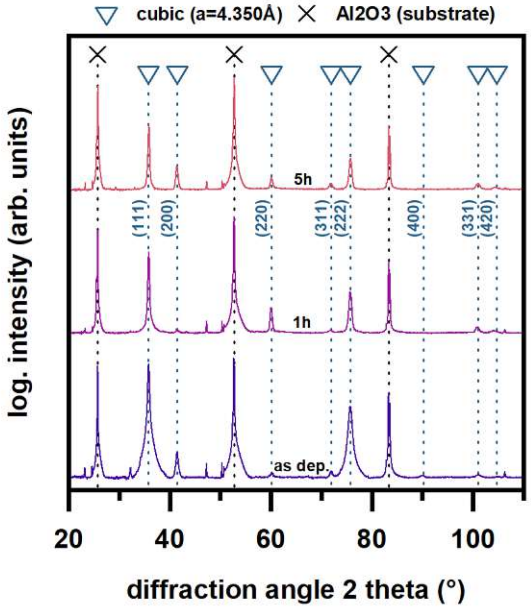

Fig. 39 X-ray diffraction patterns of silicon alloyed AlCrNbTaTi carbide thin films (2.59 at.% Si) in the as deposited state as well as oxidised at 700 °C for 1 h and 5 h. Reference data for a cubic phase (light blue triangles) as well as the Al_2O_3 substrate (black crosses) is indicated.

Yet, looking at the fracture cross-sections in Fig. 40, there is a clearly distinguishable oxide scale forming. After 1 h a thickness of the scale 370 nm is reached and it grows to 690 nm after 5 h, which is about a third of the value compared to the sample containing no silicon.

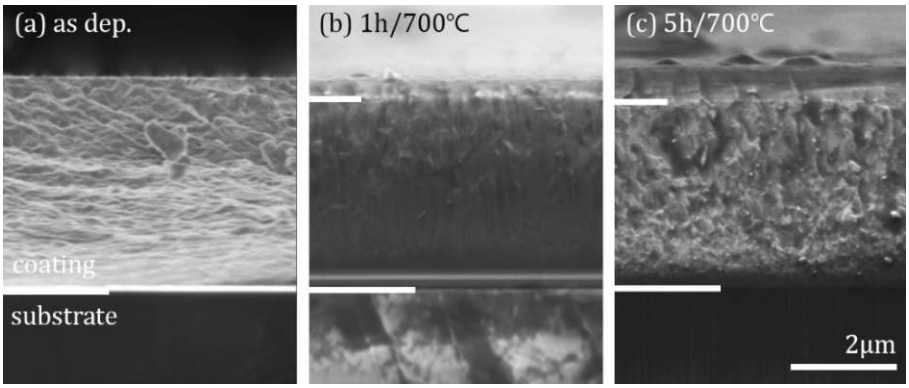

Fig. 40 SEM fracture cross-sections of silicon alloyed AlCrNbTaTi carbide thin films (2.59 at.% Si) on sapphire substrates in the (a) as deposited state as well as oxidised at 700 °C for (b) 1 h and (c) 5 h.

Interestingly, despite the impeded oxide growth rate, the sample did not withstand the annealing for 10 h. There seems to be an issue with internal stresses or the adhesion to

the substrate for this sample, which causes it to disintegrate after longer durations at elevated temperatures.

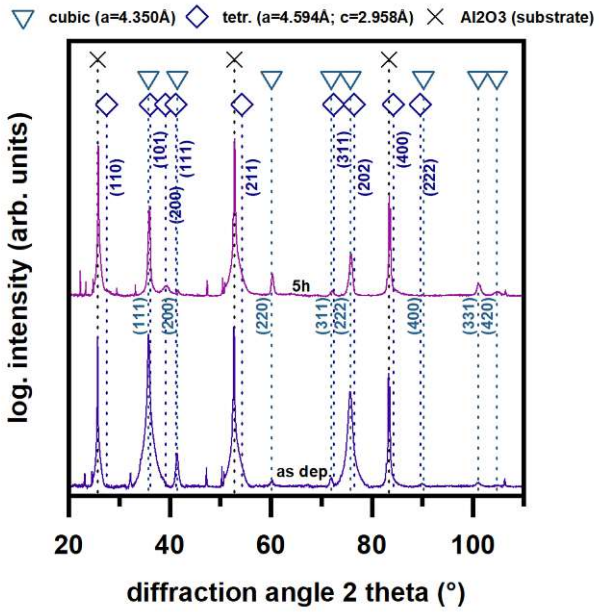

Fig. 41 X-ray diffraction patterns of silicon alloyed AlCrNbTaTi carbide thin films (2.59 at.% Si) in the as deposited state as well as oxidised at 800 °C for 5 h. Reference data for a cubic phase (light blue triangles), a tetragonal oxide phase (dark blue cubes) as well as the Al_2O_3 substrate (black crosses) is indicated.

This became apparent after ambient air annealing at 800 °C too, as only a small fraction was left on the substrate after 5 h from which the XRD pattern in Fig. 41 was recorded. There are clear tetragonal oxide peaks visible which empirically, by comparison to the other samples, implies the presence of a scale with at least several hundred nanometres in thickness. Unfortunately, the condition of the sample after annealing did not allow for the recording of a cross-section image.

The sample containing 5.98 at.% silicon does not show any new peaks till 5 h of ambient air annealing at 800 °C as shown in Fig. 42. Though, upon close inspection, there are two rutile-structured oxide peaks ((110), (101)) emerging very slightly in the 10 h pattern.

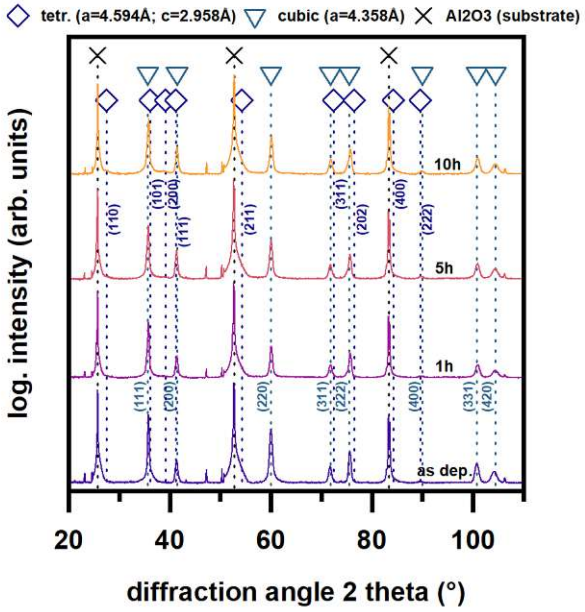

Fig. 42 X-ray diffraction patterns of silicon alloyed AlCrNbTaTi carbide thin films (5.98 at.% Si) in the as deposited state as well as oxidised at 800 °C for 1 h, 5 h and 10 h. Reference data for a cubic phase (light blue triangles), a tetragonal oxide phase (dark blue cubes) as well as the $\mathbf{Al_2O_3}$ substrate (black crosses) is indicated.

The fracture cross-sections in Fig. 43 show the formation of a 350 nm thick oxide scale after 1 h which only slightly grows to 430 nm after 10 h. This again underlines the inhibitory effect of silicon on the oxide growth and additionally a beneficial effect of silicon on the high temperature stability.

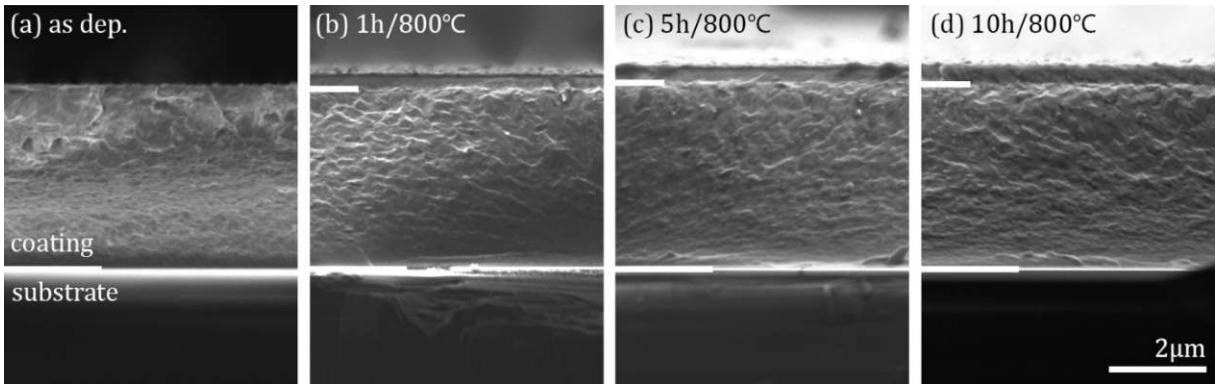

Fig. 43 SEM fracture cross-sections of silicon alloyed AlCrNbTaTi carbide thin films (5.98 at% Si) on sapphire substrates in the (a) as deposited state as well as oxidised at 800 °C for (b) 1 h, (c) 5 h and (d) 10 h.

The trend, observed in the already discussed samples, continues for the films containing 8.76 at.% silicon. Looking at the XRD patterns in Fig. 44 the films seem completely unaffected by the ambient air annealing treatments at 800 °C.

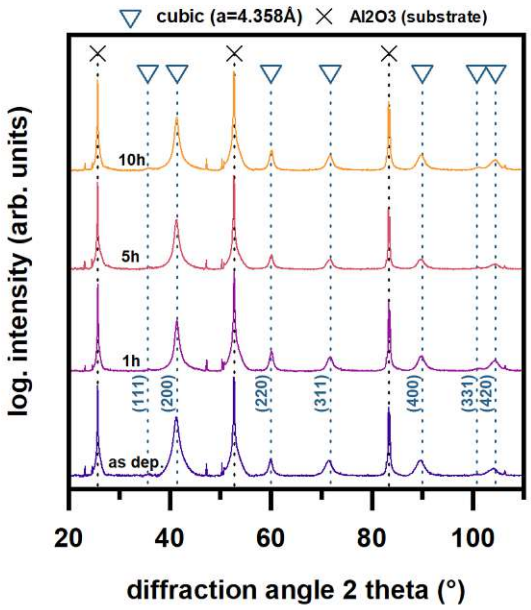

Fig. 44 X-ray diffraction patterns of silicon alloyed AlCrNbTaTi carbide thin films (8.76 at.% Si) in the as deposited state as well as oxidised at 800 °C for 1 h, 5 h and 10 h. Reference data for a cubic phase (light blue triangles) as well as the $\mathbf{Al_2O_3}$ substrate (black crosses) is indicated.

The absence of a significant oxide scale is also confirmed by the fracture cross-section images shown in Fig. 45. One could interpret the very thin lighter or darker stripes at the film surfaces as oxide scales, however those are far below the measurable range for a SEM image.

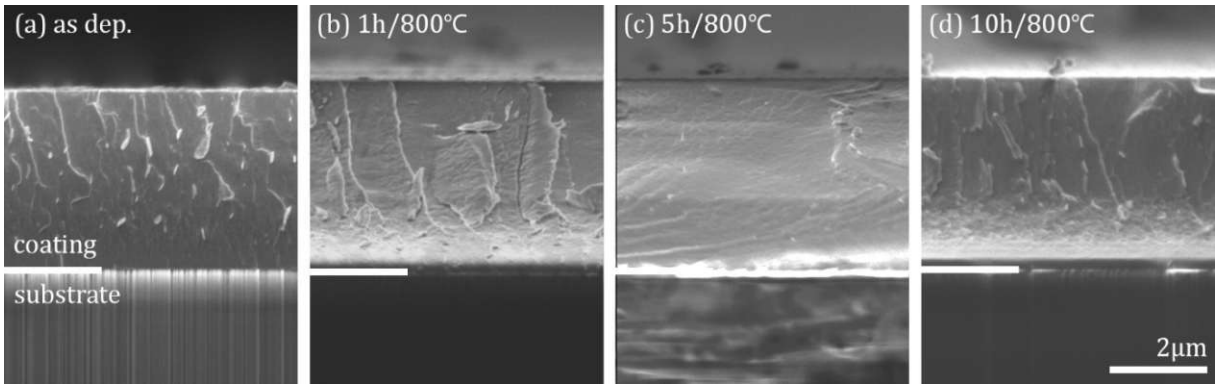

Fig. 45 SEM fracture cross-sections of silicon alloyed AlCrNbTaTi carbide thin films (8.76 at.% Si) on sapphire substrates in the (a) as deposited state as well as oxidised at 800 °C for (b) 1 h, (c) 5 h and (d) 10 h.

In Tab. 5, the thicknesses of the oxide scales and the underlying high-entropy carbide films are summarised. There again the inhibiting effect of silicon on the oxide formation is clearly recognisable.

			Oxide scale (nm)			Remaining film (nm)		
			Annealing duration (h)					
			1	5	10	1	5	10
no Si	Annealing temperature (°C)	600		190	320	4630	4390	4230
		700	450	1900	3760	4260	3760	2820
		800	7830			780		
2.59 at% Si		700	370	690		3640	3560	
5.98 at% Si		800	350	380	430	3710	3830	3830
8.76 at% Si		800		<<		4100	4100	4100

Tab. 5 Oxide scale thicknesses of the silicon alloyed AlCrNbTaTi carbide thin films after ambient air annealing treatments obtained by SEM cross-section measurements.

8 Summary and Conclusion

High-entropy carbide thin films were reactively sputtered from an equimolar AlCrNbTaTi target and additional silicon alloyed variants were synthesised. The resulting chemical composition of the films was analysed by EDX and XRF. Possible thermally-induced phase transformations or microstructural modifications and related changes in the mechanical properties were investigated by vacuum annealing treatments. Finally, the oxidation behaviour depending on the silicon content was analysed by ambient air annealing treatments inside a chamber furnace and the corresponding evaluation of SEM fracture cross-sections.

Through iterative variations in substrate temperature and reactive gas ratio a favourable process parameters were determined. At an acetylene flow rate of 20 % and a substrate temperature of 550 °C the XRD diffractograms clearly indicate the formation of a cubic solid solution phase with a cell parameter of 4.380 Å. Additionally, variants with 2.59 at.%, 5.98 at.% and 8.76 at.% silicon were synthesised. All depositions apart from the highest alloyed samples showed a preferred growth towards the (111) direction. At 8.76 at.% silicon the (200) direction is favoured, and the peak shape as well as fracture cross-section suggest a refinement of the grains in comparison to the lower alloyed films. Film thicknesses consistently showed values around 4 µm with a slight tendency to decrease with increasing silicon content.

In terms of mechanical properties, the samples showed harness values around 30 GPa with a very slight tendency to increase with silicon content. The same behaviour can generally be observed for the indentation modulus with values between 380 GPa and 450 GPa, where interestingly the sample containing 2.59 at.% silicon showed the lowest value.

Vacuum annealing treatments up to 1000 °C for each 10 minutes showed no effect on the microstructure however lead to fine cracking of the films. The lower alloyed samples disintegrated during those treatments even at 800 °C. Presumably one factor influencing this behaviour is the difference in thermal expansion between film and substrate material.

Treatments in an ambient air chamber furnace at temperatures up to 800 °C showed a strong effect of the silicon content on the oxide scale growth. The sample without silicon formed a 7.8 µm thick scale where only 780 nm of the initial film were remaining. Interestingly, the sample containing 2.59 at.% silicon showed less resilience at high temperatures than the unalloyed sample as it disintegrated for the most part at 800 °C. At 5.98

at.% Si moderate oxide growth was observed with a maximum thickness of 430 nm after 10 h at 800 °C. The maximum alloyed sample showed no visible oxide scale even after 10 h at 800 °C in ambient air.

The capabilities of the higher alloyed films were definitely not fully exploited and could be tested at even higher temperatures in future studies.

9 List of references

[1] B. Cantor, I. Chang, P. Knight and A. Vincent, Microstructural development in equiatomic multicomponent alloys, Mater. Sci. Eng. A 375–377, (2004); https://doi.org/10.1016/j.msea.2003.10.257.

[2] B. Cantor, Multicomponent and High Entropy Alloys, (2014); https://doi.org/10.3390/e16094749.

[3] J. W. Yeh, S. K. Chen, S. J. Lin, J. Y. Gan, T. S. Chin, T. T. Shun, C. H. Tsau and S. Y. Chang, Nanostructured high-entropy alloys with multiple principal elements: novel alloy design, Advanced Engineering Materials, (2004), https://doi.org/10.1002/adem.200300567.

[4] P. M. Martin, Handbook of Deposition Technologies for Films and Coatings, Elsevier, (2009); 978-0-8155-2031-3.

[5] Y. Zhang, High-Entropy Materials, Springer, (2019); https://doi.org/10.1007/978-981-13-8526-1.

[6] A. Kirnbauer , C. Spadt, C. Koller, S. Kolosvari and P. H. Mayrhofer, High-entropy oxide thin films based on Al–Cr–Nb–Ta–Ti, Vacuum - Volume 168, (2019); https://doi.org/10.1016/j.vacuum.2019.108850.

[7] A. Kretschmer, A. Kirnbauer, V. Moraes, D. Primetzhofer, K. Yalamanchili , H. Rudigier and P. H. Mayrhofer, Improving phase stability, hardness, and oxidation resistance of reactively magnetron sputtered (Al,Cr,Nb,Ta,Ti)N thin films by Si-alloying, Surface & Coatings Technology 416, (2021); https://doi.org/10.1016/j.surfcoat.2021.127162.

[8] M. C. Gao, J. W. Yeh, P. K. Liaw and Y. Zhang, High-Entropy Alloys, Springer International, (2016); https://doi.org/10.1007/978-3-319-27013-5.

[9] Y. F. Ye, Q. Wang, J. Lu, C. T. Liu and Y. Yang, High-entropy alloy: challenges and prospects, vol. 16, Materials Today, (2016); https://doi.org/10.1016/j.mattod.2015.11.026.

[10] B. Cantor, I. Chang, P. Knight and A. Vincent, “Microstructural development in equiatomic multicomponent alloys,” Materials Science and Engineering: A, (2004); https://doi.org/10.1016/j.msea.2003.10.257.

[11] H. B. Callen, Thermodynamics and an Introduction to Thermostatistics., New York: John Wiley & Sons, (1985), https://doi.org/10.1119/1.19071.

[12] Y. Zhang, Y. J. Zhou, J. P. Lin, G. L. Chen and P. K. Liaw, Solid-solution phase formation rules for multi-component alloys, vol. 10, Advanced Engineering Materials, (2008), https://doi.org/10.1002/adem.200700240.

[13] F. Otto, Y. Yang, H. Bei and E. P. George, Relative effects of enthalpy and entropy on the phase stability of equiatomic high-entropy alloys, vol. 61, Acta Materialia, (2013), https://doi.org/10.1016/j.actamat.2013.01.042.

[14] P. H. Mayrhofer, Lecture Notes: Ingenieurwerkstoffe, Vienna: Institute of Materials Science and Technology - TU Vienna, 2019.

[15] J.-W. Yeh, Recent Progress in High-Entropy Alloys, European Journal of Control, (2006); https://doi.org/10.3166/acsm.31.633-648.

[16] B. S. Murty, J. W. Yeh and S. Ranganathan, High-Entropy Alloys, Butterworth-Heinemann, (2014), https://doi.org/10.1016/C2013-0-14235-3.

[17] A. Kirnbauer, A. Kretschmer, C. Koller, T. Wojcik, V. Paneta, M. Hans, J. Schneider, P. Polcik and P. Mayrhofer, Mechanical properties and thermal stability of reactively sputtered multi-principal-metal Hf-Ta-Ti-V-Zr nitrides, Surface and Coatings Technology, Volume 389, (2020); https://doi.org/10.1016/j.surfcoat.2020.125674.

[18] D. Berardan, S. Franger, D. Dragoe, A. K. Meena and N. Dragoe, Colossal dielectric constant in high entropy oxides, Physica Status Solidi RRL, (2016), https://doi.org/10.1002/pssr.201600043.

[19] D. Berardan, S. Franger, A. K. Meenab and N. Dragoe, Room temperature lithium superionic conductivity in high entropy oxides, Journal of Materials Chemistry, (2016), https://doi.org/10.1039/C6TA03249D.

[20] P. Sigmund, Theory of Sputtering. I. Sputtering Yield of Amorphous and Polycrystalline Targets, American Physical Society, (1969); https://doi.org/10.1103/PhysRev.184.383.

[21] D. Delpa and S. Mahieu, Reactive Sputter Deposition, Ghent: Springer Berlin Heidelberg New York, (2008); https://doi.org/10.1007/978-3-540-76664-3.

[22] P. H. Mayrhofer, Lecture Notes: Surface Technology, Vienna: Institute of Materials Science and Technology - TU Vienna, (Summer Term 2022).

[23] M. Ohring, Materials Science of Thin Films (Second Edition), Elsevier, (2002); https://doi.org/10.1016/B978-0-12-524975-1.X5000-9.

[24] K. S. Sree Harsha, Principles of Vapor Deposition of Thin Films, Elsevier, (2005), https://doi.org/10.1016/B978-0-08-044699-8.X5000-1.

[25] C. R. Hogg, J. B. Kadane, J. S. Lee and S. Majetich, Error analysis for small angle neutron scattering datasets using Bayesian inference Rejoinder., Bayesian Analysis, (2010), https://doi.org/10.1214/10-BA501.

[26] M. Bouroushian and T. Kosanovic, Characterization of Thin Films by Low Incidence X-Ray Diffraction, Materials Science, (2012); https://doi.org/10.4236/csta.2012.13007.

[27] Z. Dauter and M. Jaskolski, How to read (and understand) Volume A of International Tables for Crystallography: an introduction for nonspecialists, Journal of Applied Crystallography, (2010), https://doi.org/10.1107/S0021889810026956.

[28] A. Fischer-Cripps, Critical review of analysis and interpretation of nanoindentation test data, Elsevier, (2005), https://doi.org/10.1016/j.surfcoat.2005.03.018.

[29] J.-W. Yeh, Alloy Design Strategies and Future Trends in High-Entropy Alloys, JOM 65, (2013); https://doi.org/10.1007/s11837-013-0761-6.